JACS
JOURNAL OF THE AMERICAN CHEMICAL SOCIETY

Article

pubs.acs.org/JACS

Mechanism of Assembly of the Dimanganese-Tyrosyl Radical Cofactor of Class Ib Ribonucleotide Reductase: Enzymatic Generation of Superoxide Is Required for Tyrosine Oxidation via a Mn(III)Mn(IV) Intermediate

Joseph A. Cotruvo, Jr.,[†,⊥] Troy A. Stich,[§] R. David Britt,*[,§] and JoAnne Stubbe*[,†,‡]

[†]Department of Chemistry and [‡]Department of Biology, Massachusetts Institute of Technology, 77 Massachusetts Avenue, Cambridge, Massachusetts 02139, United States

[§]Department of Chemistry, University of California, Davis, One Shields Avenue, Davis, California 95616, United States

Supporting Information

ABSTRACT: Ribonucleotide reductases (RNRs) utilize radical chemistry to reduce nucleotides to deoxynucleotides in all organisms. In the class Ia and Ib RNRs, this reaction requires a stable tyrosyl radical (Y•) generated by oxidation of a reduced dinuclear metal cluster. The Fe^{III}_2-Y• cofactor in the NrdB subunit of the class Ia RNRs can be generated by self-assembly from Fe^{II}_2-NrdB, O_2, and a reducing equivalent. By contrast, the structurally homologous class Ib enzymes require a Mn^{III}_2-Y• cofactor in their NrdF subunit. Mn^{II}_2-NrdF does not react with O_2, but it binds the reduced form of a conserved flavodoxin-like protein, $NrdI_{hq}$, which, in the presence of O_2, reacts to form the Mn^{III}_2-Y• cofactor. Here we investigate the mechanism of assembly of the Mn^{III}_2-Y• cofactor in *Bacillus subtilis* NrdF. Cluster assembly from Mn^{II}_2-NrdF, $NrdI_{hq}$, and O_2 has been studied by stopped flow absorption and rapid freeze quench EPR spectroscopies. The results support a mechanism in which $NrdI_{hq}$ reduces O_2 to $O_2^{\bullet-}$ (40−48 s^{-1}, 0.6 mM O_2), the $O_2^{\bullet-}$ channels to and reacts with Mn^{II}_2-NrdF to form a $Mn^{III}Mn^{IV}$ intermediate (2.2 ± 0.4 s^{-1}), and the $Mn^{III}Mn^{IV}$ species oxidizes tyrosine to Y• (0.08−0.15 s^{-1}). Controlled production of $O_2^{\bullet-}$ by $NrdI_{hq}$ during class Ib RNR cofactor assembly both circumvents the unreactivity of the Mn^{II}_2 cluster with O_2 and satisfies the requirement for an "extra" reducing equivalent in Y• generation.

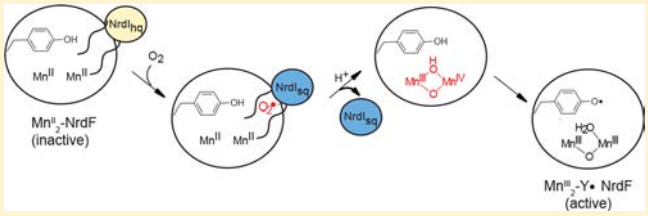

1. INTRODUCTION

Ribonucleotide reductases (RNRs) catalyze the reduction of nucleotides to their corresponding deoxynucleotides and serve as the only de novo source of the deoxynucleotides required for DNA replication and repair for all organisms.[1] RNRs are classified[2] on the basis of the stable metallocofactor required for transient generation of a cysteine thiyl radical[3,4] that initiates nucleotide reduction. In the cases of the structurally homologous class Ia and Ib RNRs, the oxidizing equivalent necessary for reversible thiyl radical generation is stored as a stable tyrosyl radical (Y•) in the enzymes' β2 subunits. The essential Y• is generated by reaction of a reduced, dinuclear metal cofactor with an oxidant. In class Ia RNRs, the active cofactor is a diferric-Y• (Fe^{III}_2-Y•), which can be assembled in vitro and in vivo using O_2 as oxidant.[5,6] Although class Ib RNRs can also assemble an active Fe^{III}_2-Y• cofactor in vitro in their β2 subunits (NrdFs), we recently discovered that an active dimanganese(III)-Y• (Mn^{III}_2-Y•) cofactor can be generated as well.[7] The relevance of the Mn^{III}_2-Y• cofactor in vivo has been demonstrated recently by purification of the NrdFs of *Corynebacterium ammoniagenes*,[8] *Escherichia coli*,[9] and *Bacillus subtilis*[10] from their native organisms; this result is likely extendable to most or all class Ib RNRs.[9] Unlike the Fe^{II}_2 forms of the class Ia and Ib RNRs, the Mn^{II}_2 form of NrdF is unreactive with O_2,[7,11] and Mn^{III}_2-Y• assembly in vitro requires a flavodoxin-like protein, NrdI, conserved in class Ib systems, in addition to O_2.[7] Here we report our efforts to elucidate the mechanism of, and essential role of NrdI in, Mn^{III}_2-Y• cofactor assembly in the *B. subtilis* class Ib RNR using stopped flow (SF) absorption and rapid freeze quench (RFQ) EPR spectroscopies.

Extensive studies of the mechanism of Fe^{III}_2-Y• cofactor assembly[12] in class Ia RNRs (Scheme 1) have provided a framework for thinking about the mechanism of Mn^{III}_2-Y• cofactor assembly. The Fe^{III}_2-Y• cofactor can be self-assembled in vitro from apo-β2, Fe^{II}, O_2, and a reducing equivalent (Scheme 2A). The diferrous form of the protein reacts with O_2 to generate a μ-peroxodiferric intermediate.[13,14] This intermediate is reduced by a neighboring tryptophan residue to form a $Fe^{III}Fe^{IV}$ intermediate, termed **X**,[15−19] and a tryptophan cation radical ($W^{+\bullet}$).[15,20,21] **X** is the species responsible for oxidation of the catalytically essential tyrosine (Y122 in *E. coli* class Ia RNR). In the presence of excess reducing equivalents (Fe^{II}, ascorbate, or thiols), this $W^{+\bullet}$ does not accumulate.[15] A protein factor, the ferredoxin YfaE in *E. coli*, is proposed to act as the donor of the extra electron in vivo.[22]

Received: December 20, 2012
Published: February 12, 2013

ACS Publications © 2013 American Chemical Society

dx.doi.org/10.1021/ja312457t | J. Am. Chem. Soc. 2013, 135, 4027−4039

Scheme 1. Mechanism of Diferric-Y• Cofactor Assembly in Class Ia RNRs

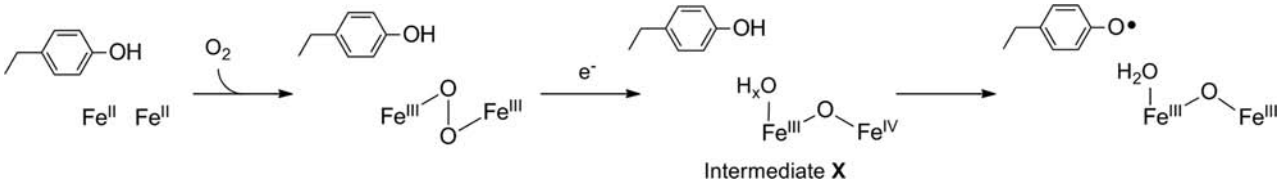

Scheme 2. (A) Stoichiometry of Diferric-Y• Cofactor Assembly in the *E. coli* Class Ia RNR, and (B,C) Proposed Stoichiometries of Dimanganese-Y• Cofactor Assembly in *E. coli* and *B. subtilis* Class Ib RNRs with H_2O_2 and $O_2^{\bullet-}$ as Oxidants

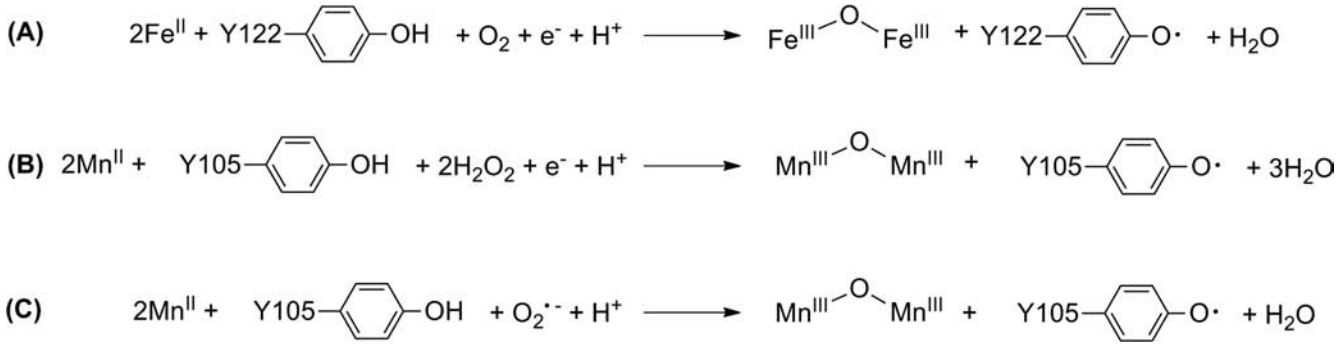

Our previous results have provided the first and, to date, only insight into the mechanism of Mn^{III}_2-Y• cofactor assembly by demonstrating that this cofactor's reconstitution in vitro requires the presence of Mn^{II}, O_2, and the reduced (hydroquinone, hq) form of NrdI.[7] Our studies of Mn^{III}_2-Y• assembly in *E. coli* suggested that NrdI reacts with O_2 to generate an oxidant competent to oxidize the Mn^{II}_2 cluster, and that this oxidant channels within a NrdI·NrdF complex from its site of production at the $FMNH^-$ cofactor of NrdI to the metal site in NrdF.[7] The channeling proposal is supported by the crystal structure of the *E. coli* NrdI·Mn^{II}_2-NrdF complex.[23] NrdI can conceivably generate either HOO(H) (represented as H_2O_2 in Scheme 2B) or $O_2^{\bullet-}$ (Scheme 2C) as oxidant; previous experiments were unable to distinguish between these options.[2,7]

Mn^{III}_2-Y• cluster is assembled in vitro with the highest yield to date in *B. subtilis* NrdF (0.6 Y•/β2),[10] providing an opportunity to monitor cluster assembly in this system by SF absorption and RFQ-EPR spectroscopies. The results of these studies, presented in this manuscript, strongly suggest that the oxidant is $O_2^{\bullet-}$, produced by reaction of $NrdI_{hq}$ with O_2, oxidizing NrdI to its neutral semiquinone (sq) form, $NrdI_{sq}$. The first metal-centered intermediate observed is a $Mn^{III}Mn^{IV}$ species, which is kinetically competent to oxidize tyrosine Y105 to Y•. This is the first catalytically relevant $Mn^{III}Mn^{IV}$ dimer in biology, and the analogue to **X** in Fe^{III}_2-Y• cofactor assembly. With $O_2^{\bullet-}$ as oxidant, the exact number of oxidizing equivalents necessary for tyrosine oxidation is provided, and the neighboring W residue does not appear to be oxidized during this process. Thus, $O_2^{\bullet-}$ is an elegant solution to both the unreactivity of the Mn^{II}_2 cluster with O_2 and the need for three oxidizing equivalents for Mn^{III}_2 formation and tyrosine oxidation.

2. EXPERIMENTAL SECTION

2.1. General Considerations. Chemical reagents and CuZn superoxide dismutase (SOD) from bovine erythrocytes (4000 U/mg) were obtained from Sigma-Aldrich at the highest purity available. Manganese concentrations were determined using a Perkin-Elmer AAnalyst 600 atomic absorption (AA) spectrometer and a Mn standard solution (Fluka). Iron quantification was carried out using the ferrozine method.[24] SF experiments were carried out using an Applied Photophysics DX 17MV instrument with the Pro-Data upgrade, using a PMT detector. RFQ experiments were performed using an Update Instruments 1019 syringe ram unit and a model 715 syringe ram controller. In both cases, the temperature was maintained at 25 °C using a Lauda circulating water bath. The temperature of the isopentane bath for RFQ was maintained using a liquid N_2 jacket and monitored using a Fluke 52II thermometer with an Anritsu Cu thermocouple probe. Calibrated EPR tubes (3.20 ± 0.01 i.d.) were from Wilmad Labglass. For anaerobic experiments, protein solutions and buffers were degassed on a Schlenk line with 5 or 6 cycles (protein) or 3 cycles (buffer) of evacuation and refilling with Ar and then brought into an anaerobic chamber (MBraun) in a cold room at 4 °C. A small amount of precipitation of both NrdI and NrdF was observed upon degassing; the solutions were centrifuged in the anaerobic chamber before use.

2.2. Protein Purification. N-Terminally His_6-tagged apoNrdF (tag: $MGSSH_6SSGLVPRGSH$) was purified as previously described,[10] with 1,10-phenanthroline added to the culture medium at 100 μM 20 min prior to induction.[25] An additional chromatographic step was added to the published procedures to increase purity and remove minor DNA contaminants. Purifications were typically carried out starting from ~24 g of cell paste (16–18 L growth). Following Ni-NTA chromatography (10 mL column, 2.5 × 2 cm), the eluent was diluted 4-fold in 50 mM Tris, 5% glycerol, pH 7.6 (Buffer A) and loaded onto a Q Sepharose column (30 mL, 2.5 × 6.5 cm) equilibrated in Buffer A containing 150 mM NaCl, which was washed with 2 column volumes of the same buffer and eluted with a 100 × 100 mL gradient of Buffer A containing 150–450 mM NaCl; 2.5–3 mL fractions were collected. ApoNrdF eluted at 280–380 mM NaCl. The pooled fractions were concentrated and exchanged into 50 mM HEPES, 5% glycerol, pH 7.6 (Buffer B), using an Amicon Ultra 30 kDa MWCO centrifugal filtration device, yielding 7–8 mg/g cell paste. ApoNrdF concentrations (expressed per β2) were assessed using ε_{280} = 110 mM^{-1} cm^{-1}.[10] ApoNrdF contained <0.01 Mn/β2 and 0.02 Fe/β2 as purified.

N-Terminally His_6-tagged NrdI (tag: $MGSSH_6SSGLVPRGSH$) was purified as described[10] with minor modifications. Following Ni-NTA chromatography, the eluent was diluted 4-fold in 50 mM sodium phosphate, 5% glycerol, pH 7.6, and loaded onto an SP Sepharose column (10 mL, 2.5 × 2 cm), which was washed with 4 column

dx.doi.org/10.1021/ja312457t | J. Am. Chem. Soc. 2013, 135, 4027–4039

volumes of Buffer B and eluted with Buffer B containing 200 mM NaCl. The eluted protein was concentrated and exchanged into Buffer B using an Amicon Ultra 10 kDa MWCO centrifugal concentrator.

2.3. Determination of the UV−Visible Spectra of NrdI in the Oxidized (ox), Neutral Semiquinone (sq), and Hydroquinone (hq) Forms. The extinction coefficient of oxidized NrdI at 449 nm in Buffer B was determined to be 12.3 mM^{-1} cm^{-1} by trichloroacetic acid precipitation as described.[26,27] From this value, the spectra of the hq and sq forms were determined as described for *E. coli* NrdI.[26]

2.4. Preparation of $NrdI_{hq}$, Mn^{II}-Loaded NrdF, and O_2-Saturated Buffer. Anaerobic solutions of NrdI (350−450 μM) were reduced by titration with a solution of sodium dithionite (5−6 mM in Buffer B) in a septum-sealed anaerobic cuvette fitted with a gastight syringe with repeating dispenser.[26] Sodium dithionite was added in 1 μL aliquots and monitored spectrophotometrically (300−800 nm) until no further change occurred. There was <5% excess dithionite in the resulting $NrdI_{hq}$ solutions.

To a solution of ∼450 μM apoNrdF was added a solution of 3−10 mM $MnCl_2$ in Buffer B (Mn concentration determined by AA spectroscopy) to a final concentration of 3.5 $Mn^{II}/\beta 2$. The protein was incubated >5 min before use. For SF experiments, the solutions were aerobic, while for RFQ-EPR experiments, the procedure was carried out in an anaerobic chamber. We denote this protein "Mn^{II}-loaded NrdF" rather than "Mn^{II}_2-NrdF" because titrations of apoNrdF with Mn^{II} monitored by EPR spectroscopy (Figure S3A) show that not all of the added Mn^{II} is bound under these conditions.

O_2-saturated Buffer B (nominally 1.3 mM O_2[28]) was prepared immediately prior to use at 23 °C by sparging with 100% O_2 in a vented container for 0.5−1 h. Where noted, SOD (section 2.1) was added to the buffer at a final concentration of 100−500 U/mL.

2.5. Fluorometric Determination of the K_d for $NrdI_{hq}$ Binding to Mn^{II}_2-NrdF. Fluorescence titration studies were carried out using a Photon Technology International QM-4-SE spectrofluorometer equipped with FELIX software and 0.5 mm excitation and 0.75 mm emission bandwidth slits. The excitation wavelength was 380 nm, and the emission data were acquired at 475−625 nm, with 1 nm steps and 0.5 s integration time.

All solutions were prepared in the anaerobic chamber. A typical experiment contained, in a final volume of 700 μL, 1 μM apo-NrdF, 4 μM $MnCl_2$, and 100 μM dithionite in Buffer B. Excess dithionite was added to ensure anaerobicity throughout the duration of the titration. This solution was placed in a semi-micro quartz fluorometer cell (10 mm path length, Starna Cells), which was sealed with a septum and screw cap. An airtight 50 μL Hamilton syringe containing 240 μM $NrdI_{hq}$ and 100 μM dithionite in Buffer B, fitted to a repeating dispenser, was inserted into the cuvette. The apparatus was removed from the glovebox and equilibrated at 23 °C for 5 min, and a baseline spectrum was recorded. $NrdI_{hq}$ was then added in 1 or 2 μL aliquots, the sample was mixed and equilibrated for 1 min, and the spectrum was recorded. The shutter was opened just before each scan and closed immediately after to minimize photobleaching. The final concentration of $NrdI_{hq}$ was 15 μM. Data were analyzed by the method of Eftink,[29] described in detail in the Supporting Information (SI, section S1.1), to provide the stoichiometry of NrdI binding (n) and the K_d for its interaction with NrdF.

2.6. Kinetics of Mn^{III}_2-$Y^\bullet$ Cofactor Assembly Monitored by Stopped-Flow Absorption Spectroscopy. SF kinetics experiments were carried out at 25 ± 1 °C, maintained using a Lauda circulating water bath. The SF apparatus is in the open air; to minimize O_2 contamination, the connections of the syringes were purged continuously before and during the experiment with N_2, and prior to the experiment, the SF lines were rinsed with 10 mL of 300 mM dithionite followed by 25−30 mL of anaerobic Buffer B. In a typical experiment, 20 μM $NrdI_{hq}$ in Buffer B, prepared anaerobically in one gastight Hamilton syringe, was mixed in a 1:1 ratio with O_2-saturated Buffer B (1.3 mM O_2) and 500 U/mL SOD (section 2.1), or O_2-saturated Buffer B and 50 μM Mn^{II}-loaded NrdF (3.5 Mn^{II}/NrdF), in a second syringe. The reaction was monitored at single wavelengths (340, 410, or 610 nm), 4 or 5 shots were collected and averaged, and the experiments were repeated 2 or 3 times. Reactions were also monitored from 310 to 700 nm in 10 nm intervals (one shot per wavelength, performed on five separate occasions and each data set analyzed independently). After blanking the instrument at each wavelength, a zero time point spectrum was obtained by mixing 20 μM $NrdI_{hq}$ 1:1 with anaerobic Buffer B. Global analysis of the multiwavelength SF data was carried out in KinTek Explorer v.3.0 with SpectraFit.[30,31]

For studies of the O_2 dependence of the cluster assembly reaction, 25%, 50%, and 75% O_2-saturated buffer (0.3, 0.6, and 0.9 mM O_2) was prepared by drawing the appropriate amount of O_2-saturated buffer into a gastight syringe containing anaerobic buffer. The contents were mixed and loaded immediately to the SF apparatus.

2.7. Kinetics of Mn^{III}_2-$Y^\bullet$ Cofactor Assembly Monitored by Rapid Freeze Quench EPR Spectroscopy. In a typical experiment, Mn^{II}_2-NrdF (150 μM, 3.5 $Mn^{II}/\beta 2$) and $NrdI_{hq}$ (100 μM)[32] in Buffer B in one syringe, prepared in the anaerobic box, was mixed with O_2-saturated Buffer B in the second syringe in a 1:1 ratio at 25 °C and aged for a predetermined time period (6 ms−60 s) in the reaction loop. The reaction mixture (350−400 μL) was sprayed, using a drive ram velocity of 1.25−3.2 cm/s,[33] into liquid isopentane at −140 ± 5 °C in a glass funnel attached to an EPR tube.[34] The samples were packed into the EPR tubes using a stainless steel rod and stored in liquid N_2 until analysis. Under these conditions, no decay of $NrdI_{sq}$ and the $Mn^{III}Mn^{IV}$ intermediate was observed during storage for 1 month, but ∼20−30% decay of both signals was observed over 7 months. The quench times stated in the Results (12 ms−60 s) include the time required to pass through the reaction loop after mixing plus 6 ms for quenching (estimated as described in ref 35). The packing factor for NrdF was determined to be 0.55 ± 0.03 using Fe^{III}_2-$Y^\bullet$ NrdF in Buffer B, prepared as described.[10]

2.8. Determination of the UV−Visible Absorption Spectra of the Mn^{III}_2 Cluster and the $Y^\bullet$. *2.8.1. Preparation of Mn^{III}_2-$Y^\bullet$ NrdF.* Protein solutions from 12 RFQ reactions quenched at ≥48 ms (section 2.7, 7 mL total volume) were recovered from the reaction loops, pooled, and incubated on ice for 30 min with 5 mM EDTA. The mixture was then loaded onto a Q Sepharose column (3 mL, 1 × 3.5 cm) pre-equilibrated in Buffer B containing 100 mM NaCl, and the column was washed with 9 mL of the same buffer. NrdI eluted in the loading and wash fractions. NrdF was eluted with 4 mL of Buffer B containing 500 mM NaCl. Protein-containing fractions were pooled/concentrated and repeatedly diluted with Buffer B until the concentration of NaCl was <10 mM. The isolated Mn^{III}_2-$Y^\bullet$ NrdF contained 1.0 $Mn/\beta 2$ and 0.36 ± 0.01 $Y^\bullet/\beta 2$. Thus, for a reaction mixture containing 75 μM Mn^{II}-loaded NrdF and 50 μM NrdI, 75 μM Mn is oxidized, 27 μM $Y^\bullet$ is generated, and 21 μM Mn^{III} is not associated with $Y^\bullet$.

2.8.2. Reduction of $Y^\bullet$ Using Hydroxylamine and Extinction Coefficient Determination of Mn^{III}_2 Cluster. Hydroxylamine and hydroxyurea reduce $Y^\bullet$ and, albeit more slowly, the Mn^{III}_2 cluster.[7] Thus, determination of the individual spectra of the Mn^{III}_2 cluster and $Y^\bullet$ requires measurement of the UV−vis spectra of NrdF before and after hydroxylamine treatment, accompanied by determination of the $Y^\bullet$ concentration by EPR spectroscopy and the Mn concentration by AA spectroscopy. The detailed procedure is given in section S1.2.

2.9. Electron Paramagnetic Resonance Spectroscopy. The concentrations of $Y^\bullet$ and $NrdI_{sq}$ were determined on a Bruker EMX X-band spectrometer at 77 K using a quartz finger dewar. Analysis of $Y^\bullet$ has been described.[7] Analysis of the sq was carried out at 77 K using the following parameters: 9.34 GHz frequency, 5 μW power, 5 × 10^4 gain, 100 kHz modulation frequency, 0.15 mT modulation amplitude, 5.12 ms time constant, and 20.48 ms conversion time. Spin quantitation of both $Y^\bullet$ and sq was carried out using an *E. coli* Fe^{III}_2-$Y^\bullet$ NrdF standard calibrated against a Cu^{II} perchlorate standard.[36]

Other EPR spectra were measured at the CalEPR Center at the University of California, Davis. Continuous-wave (CW) X-band spectra were acquired with an ECS106 or E-500 spectrometer (Bruker, Billerica, MA) under non-saturating slow-passage conditions using a Super-High Q resonator (ER 4122SHQE). Cryogenic temperatures were achieved and maintained using an Oxford

Scheme 3. Proposed Mechanism of Mn^{III}_2-$Y^{\bullet}$ Cofactor Assembly in *B. subtilis* NrdF[a]

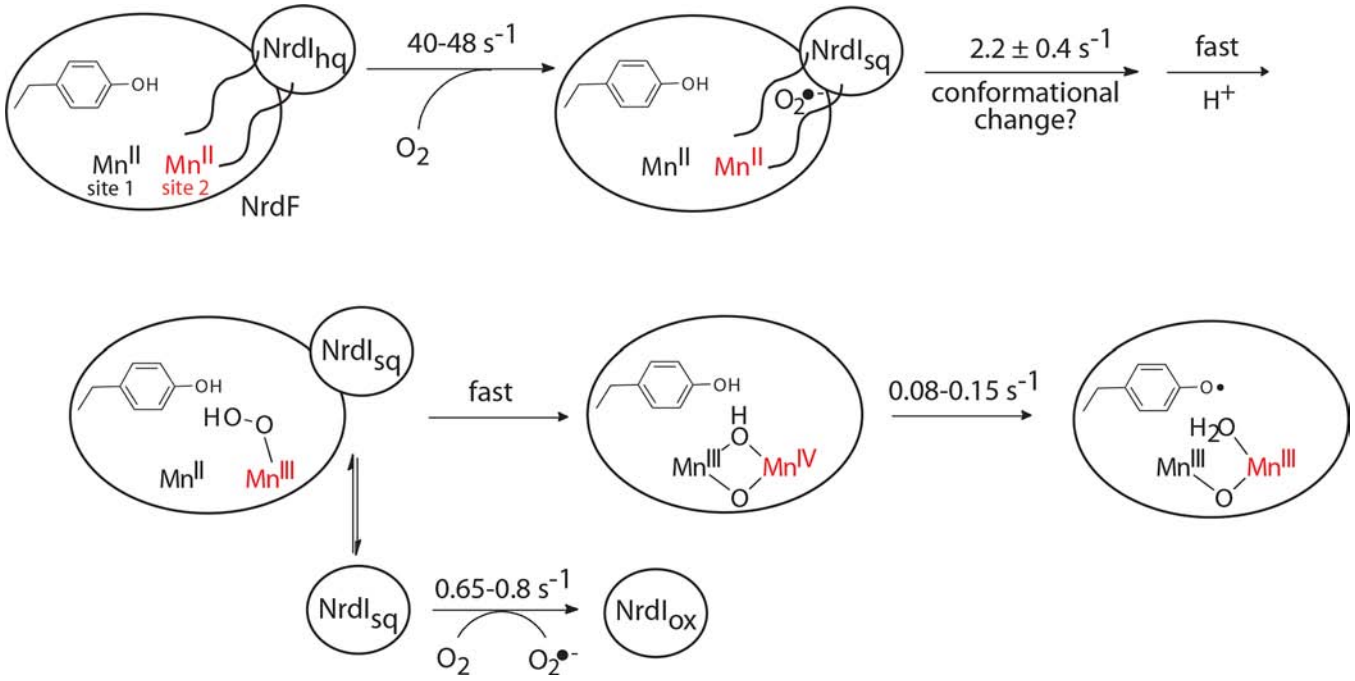

[a]Rate constants were measured in this study. The detailed structures of the proposed $Mn^{II}Mn^{III}$–OO(H) and $Mn^{III}Mn^{IV}$ intermediates, as well as the oxidation state of NrdI when it dissociates from NrdF, are unknown. Mn at site 1 (Mn1) is closest to the Y that is oxidized; Mn2 is indicated in red.

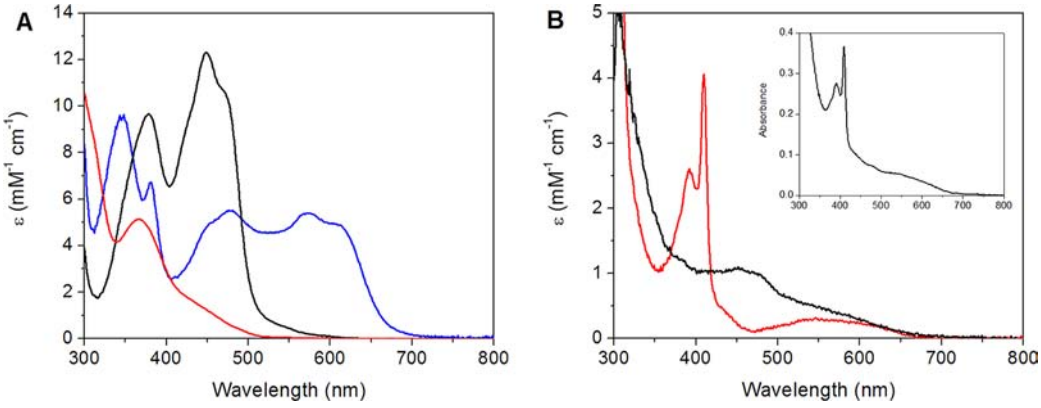

Figure 1. UV–vis absorption spectra of NrdI and NrdF. (A) $NrdI_{ox}$ (black), $NrdI_{sq}$ (neutral form, blue), and $NrdI_{hq}$ (red). The sq spectrum was estimated as described in section 2.3. (B) The $Y^{\bullet}$ (red) and Mn^{III}_2 cluster (black, εs given for cluster following $Y^{\bullet}$ reduction) in NrdF, after removal of the contribution of protein end absorption. Inset: 200 μM Mn^{III}_2-$Y^{\bullet}$ NrdF, containing 1.0 Mn/β2 and 0.36 $Y^{\bullet}$/β2.

Instruments ESR900 liquid helium cryostat in conjunction with an Oxford Instruments ITC503 temperature and gas flow controller. Spectral simulations were performed with Matlab using the EasySpin 4.0 toolbox.[37]

Quantification of the unpaired spin concentration within a sample was achieved by comparison of the double integral of the EPR intensity to that of a standard solution of 308 μM Cu^{II} in 100 mM EDTA, pH 6.2. Due to the presence of multiple paramagnetic species in the RFQ samples, double integration of each of the individual components was not possible. In the case of the transiently generated $Mn^{III}Mn^{IV}$ species, a simulated spectrum was scaled until the integrated intensity of peaks 11–14 (ca. 349, 358, 365, and 373 mT, see Figure 6) matched that of the experimental spectrum. The entirety of the scaled simulated spectrum was then doubly integrated and compared to the spin standard.

2.10. Determination of Rate Constants of NrdI Comproportionation and Disproportionation by SF Absorption Spectroscopy. NrdI was reduced by anaerobic titration with sodium dithionite as described previously,[26] and the SF apparatus was prepared as described in section 2.6. In a typical experiment, one syringe contained 20 μM $NrdI_{hq}$ in Buffer B, and the second contained an anaerobic solution of 20 μM $NrdI_{ox}$ either alone or with 80 μM apoNrdF. The reactions were monitored at 25 °C at 610 nm from 1.5 ms to either 15 s or 200 s, respectively. At least three replicate traces were collected and averaged in three separate experiments and analyzed using KinTek Explorer v.3.0 according to eq 4 (section 3.5).

2.11. Analysis of Kinetics Data. Nonlinear least-squares fitting of single-wavelength data from SF and RFQ-EPR experiments to sums of single exponentials was carried out using Origin (Microcal) or KaleidaGraph (Synergy Software). All other kinetic analysis used KinTek Explorer v.3.0 with SpectraFit.[30,31]

3. RESULTS

3.1. Proposed Model for Mn^{III}_2-$Y^{\bullet}$ Assembly. Here, we describe rapid kinetics studies using SF absorption and RFQ-EPR spectroscopies to determine the mechanism by which NrdI is involved in Mn^{III}_2-$Y^{\bullet}$ cofactor assembly in the *B. subtilis*

class Ib RNR. Our studies have led to the working model in Scheme 3. Specifically, our evidence described subsequently supports (1) rapid one-electron reduction of O_2 by $NrdI_{hq}$ to generate $O_2^{\bullet-}$ (40−48 s^{-1}); (2) slower formation of a $Mn^{III}Mn^{IV}$ intermediate (2.2 ± 0.4 s^{-1}) subsequent to $O_2^{\bullet-}$ production; and (3) decay of the $Mn^{III}Mn^{IV}$ intermediate concomitant with $Y^{\bullet}$ generation (0.08−0.15 s^{-1}).

3.1.1. Information Required for Experimental Design and Spectral Deconvolution. To design the SF and RFQ-EPR experiments that led to Scheme 3, a number of parameters were determined for the NrdI/NrdF system. First, the UV−vis absorption and EPR spectra (where appropriate) of starting materials and products were obtained. Second, a knowledge of the affinity between $NrdI_{hq}$ and Mn^{II}_2-NrdF is required to maximize complex formation. Third, because minimal studies of the reaction of flavodoxins with O_2, and no studies of the reaction of NrdIs with O_2, have been reported, the reaction of $NrdI_{hq}$ with O_2 was assessed. The results of these experiments are described first.

3.2. UV−Visible Absorption Spectra of NrdI, Mn^{III}_2-NrdF, and $Y^{\bullet}$. Analysis of the SF data requires knowledge of the UV−vis absorption spectra of the stable redox states of NrdI and NrdF. The UV−vis absorption spectra of NrdI in hq, sq, and ox states are shown in Figure 1A. Because NrdI accumulates only 30% sq during anaerobic titration with sodium dithionite,[10] the spectrum of $NrdI_{sq}$ was estimated by correlation of UV−vis and EPR spectra of solutions of NrdI partially reduced with known amounts of dithionite. The spectrum is similar to those of flavodoxins and other NrdIs.[26,27,38] $NrdI_{sq}$ is entirely in the neutral form under the conditions used in all experiments (pH 7.6), based on UV−vis, EPR, and SF absorption experiments (section S2.1, Table S1, and Figure S1).

The UV−vis absorption spectrum of NrdF reconstituted with Mn^{III}_2-$Y^{\bullet}$ cofactor is shown in the inset of Figure 1B. Figure 1B also shows the spectrum resolved into its two components, the Mn^{III}_2 cluster and the $Y^{\bullet}$. To obtain these spectra, Mn^{III}_2-$Y^{\bullet}$ NrdF (200 μM) was incubated with hydroxylamine (0.5 mM) (sections 2.8 and S1.2). The deconvolution is complicated as $Y^{\bullet}$ reduction is accompanied by slower reduction of the Mn^{III}_2 cluster.[7] By 10 min, when $Y^{\bullet}$ is fully reduced, ∼60% of the Mn is also reduced, based on AA analysis of NrdF subsequent to chelation with EDTA and Sephadex G25 chromatography to remove Mn^{II}-EDTA. The spectrum of $Y^{\bullet}$ was then determined by spectral subtractions and the quantification of $Y^{\bullet}$ by EPR spectroscopy. The spectrum of the Mn^{III}_2 cluster exhibits a weak, broad feature at 460 nm with a shoulder at 485 nm, similar to the Mn^{III}_2 form of Mn catalase, whose active site is structurally related to that of the class I RNRs.[39] The spectrum of $Y^{\bullet}$ exhibits a diagnostic, sharp peak at 410 nm, a shoulder at 392 nm, and a broad feature from 470 to 670 nm. The analysis indicated that the UV−vis absorption spectrum intensity of the Mn^{III}_2 cluster increased by 190% upon reduction of Mn^{III}_2-$Y^{\bullet}$ cofactor to Mn^{III}_2 cluster (Figure S2). Similar 2−3-fold changes in absorption intensities of biological Mn complexes have also been reported for anion binding to Mn-SOD[40] and for mutation of a tyrosine in the second coordination sphere of Mn catalase.[41] These changes have been assigned to structural reorganizations, which suggests that, in NrdF, $Y^{\bullet}$ reduction may alter the coordination sphere of the accompanying Mn^{III}_2 cluster. The absorption spectrum of Mn^{II}-loaded NrdF (not shown) is identical to that of apo-NrdF, featureless in the visible region.

3.3. EPR Spectra of Mn^{II}-Loaded NrdF, Mn^{III}_2-$Y^{\bullet}$ NrdF, and $NrdI_{sq}$. Characterization of the EPR spectra of Mn^{II}-loaded and Mn^{III}_2-$Y^{\bullet}$ NrdF is important for the RFQ-EPR analysis of the cluster assembly reaction described below. The EPR spectrum of $NrdI_{sq}$ (77 K, Figure S1) is similar to previously described flavodoxin neutral sqs.[42]

3.3.1. Mn^{II}-Loaded NrdF. Initially, NrdF was loaded with Mn^{II} following the protocol reported for *E. coli* NrdF,[7] by incubation of the apoprotein with 4 $Mn^{II}/\beta 2$ followed by passage through a Sephadex G25 column to remove unbound Mn^{II}. For *E. coli* NrdF, this procedure yielded protein with a complex, multiline (∼40 lines) EPR signal with negligible amounts of mononuclear Mn^{II}.[7] However, when this same protocol was followed for *B. subtilis* NrdF, its EPR signal revealed a substantial contribution from mononuclear Mn^{II} in addition to a signal associated with a coupled Mn^{II}_2 cluster. Titrations of 75 μM apoNrdF with Mn^{II}, monitored by EPR spectroscopy at 10 K, show that the mononuclear Mn^{II} is present even at 1 $Mn^{II}/\beta 2$ (Figure S3A). Measurements at 293 K, where only unbound Mn^{II} is detectable, suggest that <10% of the total Mn^{II} is unbound at 3.5 $Mn^{II}/\beta 2$, whereas 20% is unbound at 4.0 $Mn^{II}/\beta 2$. Therefore, to minimize the unbound Mn^{II} present, EPR samples were generally prepared using 3.5 $Mn^{II}/\beta 2$ (Figure 2A). Similar titrations of *E. coli* apoNrdF exhibit negligible unbound Mn^{II} unless the $Mn^{II}/\beta 2$ is greater than 3.5, indicating much stronger Mn^{II} binding than to *B. subtilis* NrdF (Figure S3B).

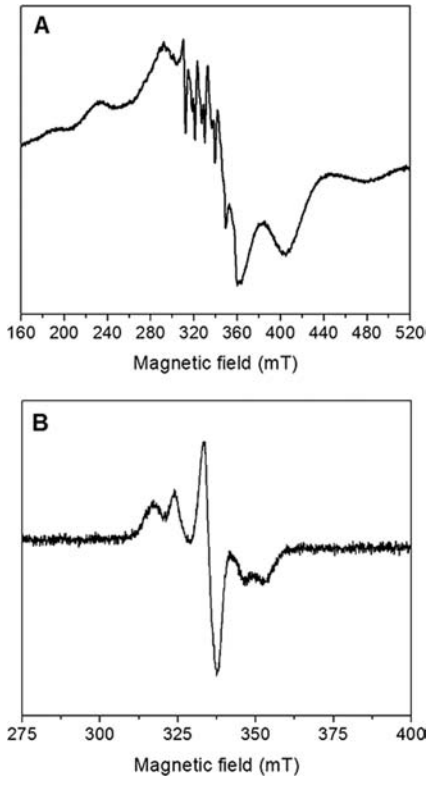

Figure 2. X-band EPR spectra of (A) Mn^{II}-loaded NrdF (150 μM NrdF, 3.4 $Mn^{II}/\beta 2$, acquired at 0.1 mW, 10 K), (B) Mn^{III}_2-$Y^{\bullet}$ NrdF (0.1 mW, 10 K). Other acquisition parameters are described in section 2.9.

dx.doi.org/10.1021/ja312457t | J. Am. Chem. Soc. 2013, 135, 4027−4039

As for the Mn^{II}_2 cluster of *B. subtilis* NrdF itself, the low-temperature X-band CW EPR spectrum possesses several resonances (Figures 2A, S4) across the explored field range (0−900 mT). The features at 270−300 and 380−440 mT show evidence of hyperfine structure with splittings of approximately 4.2 mT. Such a splitting pattern is consistent with nearly equal hyperfine interactions (HFIs) from two exchange-coupled $^{55}Mn^{II}$ (I = 5/2) ions [$A(^{55}Mn)$ = 285 MHz, typically].[43,44] As the temperature is raised, the total integrated intensity of the EPR spectrum increases (Figure S4, inset). This behavior indicates that the two Mn^{II} ions are antiferromagnetically coupled (i.e., that J < 0; using the Heisenberg−Dirac−van Vleck Hamiltonian for exchange $\hat{H} = -2JS_1S_2$) and, at higher temperatures, higher energy spin manifolds on the spin-ladder become thermally populated at the expense of the EPR-silent S_T = 0 ground spin level.

3.3.2. Mn^{III}_2-Y• NrdF. The EPR spectrum of *B. subtilis* Mn^{III}_2-Y• NrdF (10 K, Figure 2B) is similar to that of *E. coli* NrdF.[7] The five-line pattern present in the low-temperature EPR spectra of the Mn^{III}_2-Y• cofactors of class Ib RNRs has been attributed to the interaction of Y• with the Mn^{III}_2 cluster.[8] As the temperature is increased, the signal appears to collapse, yielding, at 100 K, what appears to be a spectrum of solely a Y• (Figure S5). Similar temperature-dependent behavior has been observed for a nitroxide coupled to a ferric-heme complex[45] and for the acetate-inhibited S_2-form of photosystem II (in this case, a Y• is coupled to a paramagnetic tetranuclear Mn cluster).[46] With increasing temperature, the rate of electronic relaxation of the metal-based paramagnet increases and decouples this spin center from the nearby organic radical. This decoupling removes any contribution to the spectrum from dipolar and/or exchange interactions between the two spin centers. Thus, the high-temperature spectrum of NrdF described here is essentially that of Y• isolated from the Mn^{III}_2 cluster.

As a result of this decoupling, the structure evident in the 100 K spectrum can be assigned as HFI of the unpaired electron on tyrosine with four protons: those at the 3 and 5 positions of the phenoxyl ring, and the two bound to the β-carbon of the side chain. To simulate this spectrum, the HFI for H3/5 were held fixed at values typically found for Y•'s in class Ib RNRs (section S2.2).[47] The contribution to the spectrum by the two β-protons was determined using the McConnell relations by varying the value of the dihedral angle Θ[48] until the simulated spectrum best agrees with the experimental one.[49] This was achieved with an angle of 44(±2)°, slightly larger than the dihedral angles of 25 and 32° observed in the two chains of the crystal structure of *B. subtilis* Mn^{II}_2-NrdF (see Figure S6 for a comparison of simulations achieved using these other values of Θ).[50] This increase in dihedral angle observed for Mn^{III}_2-Y• compared to that found in the structure of the Mn^{II}_2 form suggests that the phenoxyl plane has rotated with respect to the β-carbon upon oxidation of NrdF in the presence of NrdI and O_2. Interestingly, in the crystal structure of the Mn^{III}_2 form of *C. ammoniagenes* NrdF, the tyrosine adjacent to the Mn cluster (Y115) has a dihedral angle of 40° and 42° in the first and second chains, respectively.

3.4. K_d for $NrdI_{hq}$ and Mn^{II}_2-NrdF. Knowledge of the affinity of $NrdI_{hq}$ for Mn^{II}_2-NrdF is also important to maximize complex formation in the rapid kinetics studies described subsequently. To make this measurement, we took advantage of the previous observation that the hq forms of flavodoxins display weak fluorescence with a broad excitation maximum centered at ∼370 nm and emission maxima in the 500−530 nm region.[51] Our initial experiments demonstrated that the $NrdI_{hq}$ $FMNH^-$ cofactor displays similar fluorescence properties and that the intensity of its fluorescence emission spectrum is sensitive to the presence of NrdF (Figure S7A); this property was exploited to determine the K_d for $NrdI_{hq}$ binding to Mn^{II}_2-NrdF. A control titration of *B. subtilis* $NrdI_{hq}$ with *E. coli* Mn^{II}_2-NrdF exhibited no change in fluorescence, demonstrating that this method reports on specific NrdI-NrdF interactions. Titrations of Mn^{II}-loaded *B. subtilis* NrdF (1 μM, 4 $Mn^{II}/\beta 2$) with $NrdI_{hq}$ were analyzed using a non-cooperative binding model, as described in the SI (section S1.1, Figure S7B). The analysis gives 1.6 ± 0.1 NrdI per NrdF dimer with K_d = 0.6 ± 0.2 μM. Figures 2A and S3A suggest that NrdF is not fully loaded with Mn^{II} under these conditions, but a similar K_d was obtained with apoNrdF. The unusual binding stoichiometry may therefore indicate error in the computationally derived extinction coefficient of NrdF,[52] or that a fraction of NrdF is incompetent to bind NrdI. This K_d value is significantly lower than that previously reported for *B. anthracis* $NrdI_{ox}$·NrdF, 23 μM.[53] The sequence similarity between the *B. subtilis* and *B. anthracis* systems (75% for NrdF, 63% for NrdI) suggests that the difference in K_d values reflects tighter binding of NrdF to $NrdI_{hq}$ than to $NrdI_{ox}$. The K_d of 0.6 μM indicates that, at the concentrations of NrdF and $NrdI_{hq}$ used in subsequent rapid kinetics experiments, >95% of $NrdI_{hq}$ is complexed.

3.5. Reaction of $NrdI_{hq}$ with O_2 (±NrdF) Monitored by SF Absorption. Typical flavodoxins react with O_2 to produce $O_2^{\bullet-}$;[54,55] however, based on the unusual redox properties of *E. coli*[26] and *B. subtilis*[10] NrdIs, we previously proposed that $NrdI_{hq}$ would react with O_2 to produce H_2O_2. To resolve this issue, and as a prelude to our investigation of the kinetics of Mn^{III}_2-Y• cofactor assembly from $NrdI_{hq}$, Mn^{II}_2-NrdF, and O_2, we initially investigated the kinetics of the reaction of $NrdI_{hq}$ alone with O_2.

In these experiments, 20 μM $NrdI_{hq}$ and O_2-saturated buffer (1.3 mM O_2) were mixed in a 1:1 ratio at 25 °C, in the presence of 250 U/mL SOD, and the reaction was monitored by SF absorption spectroscopy from 310 to 700 nm at 10 nm increments. SOD was included to minimize kinetic complexity associated with production of $O_2^{\bullet-}$, which can also react with $NrdI_{hq}$ and $NrdI_{sq}$ (section S2.3).[55] Singular value decomposition (SVD) analysis of the data indicated significant contribution from three absorbing species: $NrdI_{hq}$ (E-$FMNH^-$), $NrdI_{sq}$ (E-$FMNH^{\bullet}$), and $NrdI_{ox}$ (E-FMN). The data were fit using the global analysis software KinTek Explorer v.3.0 with SpectraFit in order to extract the spectra of these species. The ability to reproduce the known $NrdI_{sq}$ spectrum (Figure 1A) was one of the criteria used to judge the appropriateness of the kinetic model. The full analysis is described in section S2.3 (Figures S8A and S9). Three reactions (eqs 1−3) were required in the kinetic model to reproduce the known $NrdI_{sq}$ spectrum.

$$\text{E-FMNH}^- + O_2 \xrightarrow{k_1} \text{E-FMNH}^{\bullet} + O_2^{\bullet-} \quad (1)$$

$$\text{E-FMNH}^{\bullet} + O_2 \xrightarrow{k_2} \text{E-FMN} + O_2^{\bullet-} \quad (2)$$

$$\text{E-FMNH}^- + O_2 \xrightarrow[H^+]{k_3} \text{E-FMN} + H_2O_2 \quad (3)$$

This model gives rate constants of k_1 = 1.6 ± 0.1 mM^{-1} s^{-1}, k_2 = 2.0 ± 0.1 mM^{-1} s^{-1}, and k_3 = 0.7 ± 0.1 mM^{-1} s^{-1}, for eqs 1, 2, and 3, respectively. Based on this model and the relative

values of k_1 and k_3, 70% of $NrdI_{hq}$ reacts with O_2 to initially form $NrdI_{sq}$ and $O_2^{\bullet-}$. The $NrdI_{sq}$ then goes on to react with O_2 to produce $NrdI_{ox}$ and $O_2^{\bullet-}$. Thirty percent of $NrdI_{hq}$ reacts by a second pathway to form $NrdI_{ox}$ and H_2O_2.

To investigate whether complexation with NrdF affects the kinetics of $NrdI_{hq}$ oxidation, SF experiments were also carried out with $NrdI_{hq}$ (20 μM) mixed in a 1:1 ratio with O_2-saturated buffer containing NrdF (50 μM, 98% complex), apo or Mn^{II}-loaded, and SOD. Unlike the reaction of $NrdI_{hq}$ with O_2, these SF data could not be satisfactorily modeled by the reactions in eqs 1−3, although SVD again indicated the presence of only three spectrally distinct species. Therefore, we instead focused on the pseudo-first-order rate constants for $NrdI_{sq}$ formation and decay, which can be extracted directly from SF traces acquired at 610 nm, where only $NrdI_{sq}$ contributes significantly (Figures 1A and 3). $NrdI_{sq}$ formation is accelerated in the presence of apoNrdF and even further accelerated in the presence of Mn^{II}-loaded NrdF (Figure 3). Whereas the A_{610} SF traces for reaction of $NrdI_{hq}$ alone with O_2 can be fit to a sum of two exponentials, those in the presence of NrdF are best fit to three exponentials, with two phases required for sq formation and one phase for sq decay (Table 1, Figure S10). We attribute the presence of two phases for sq formation to interaction of NrdI with conformationally heterogeneous populations of NrdF (note that even in the presence of Mn^{II}-loaded NrdF, only 80% of NrdF contains Mn^{II}_2 cluster). The rate constants for the major phases (75−80% of total amplitude) of sq formation in the presence of apo- and Mn^{II}-loaded NrdF were 5 and 25 times faster, respectively, than that for $NrdI_{sq}$ formation in the absence of NrdF. The sensitivity of the rate constants for $NrdI_{sq}$ formation to the presence of NrdF and Mn^{II} suggests the relevance of eq 1 to Mn^{III}_2-$Y^{\bullet}$ cofactor assembly, discussed subsequently. By contrast, the rate constant for $NrdI_{sq}$ decay (eq 2) was very similar in the presence and absence of NrdF (Table 1).

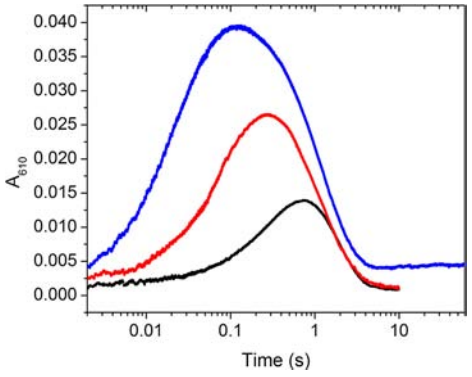

Figure 3. Comparison of representative A_{610} traces for reaction of 20 μM $NrdI_{hq}$ mixed 1:1 with O_2-saturated buffer containing no NrdF (black), 50 μM apo-NrdF (red), and 50 μM Mn^{II}-loaded NrdF (blue, 3.5 $Mn^{II}/\beta 2$). The first and second reactions also contained SOD (100 U/mL). The reactions were carried out at 25 °C, pH 7.6. The small increase at >5 s in the blue trace is due to Mn^{III}_2-$Y^{\bullet}$ cofactor assembly.

Table 1. Apparent Rate Constants (Amplitudes in Parentheses) for the Fits to the SF Traces Shown in Figure 3

	k (s^{-1})		
phase	NrdI[a]	NrdI + apoNrdF[a]	NrdI + Mn^{II}-loaded NrdF[b]
sq formation (major phase)	1.6 (0.052)	7.4 (0.026)	42 (0.039)
sq formation (minor phase)	NA[c]	18 (0.009)	5.4 (0.008)
sq decay (eq 2)	1.1 (−0.053)	0.93 (−0.035)	0.85 (−0.049)

[a]100 U/mL SOD. [b]No SOD. [c]Not applicable (phase not observed).

Control experiments indicated that comproportionation and disproportionation reactions (eq 4) of NrdI's FMN cofactor were too slow to contribute significantly to the overall reactions of NrdI with O_2 in the presence and absence of NrdF (section S2.4, Figure S11, Table S2). This observation indicates that the acceleration in $NrdI_{sq}$ formation in the presence of NrdF is due to an increase in k_1, rather than a large increase in k_3 followed by comproportionation. Therefore, the data suggest that the reaction of $NrdI_{hq}$ with O_2 to produce $NrdI_{sq}$ and $O_2^{\bullet-}$ also predominates in the presence of apo- or Mn^{II}-loaded NrdF.

$$\text{E-FMNH}^{-} + \text{E-FMN} \underset{k_{-4}}{\overset{k_{+4}}{\rightleftharpoons}} 2\text{E-FMNH}^{\bullet} \quad (4)$$

3.6. Mn^{III}_2-$Y^{\bullet}$ Cofactor Assembly Monitored by SF Absorption and RFQ-EPR Spectroscopies. The experiments described above provided the information required to design the central experiment: the reaction of $NrdI_{hq}$ with O_2 in the presence of Mn^{II}-loaded NrdF, monitored by SF absorption and RFQ-EPR spectroscopies.[56] The experimental design is challenging, as it is necessary to minimize excess Mn^{II}, which interferes with the EPR analysis, and to maximize $NrdI_{hq}$-NrdF complex formation, to avoid free $NrdI_{hq}$ reacting with O_2. As described in section 3.3 (Figure S3A), adding 3.5 $Mn^{II}/\beta 2$ to 75 μM apoNrdF strikes a balance between high metal loading of NrdF (3.2 $Mn^{II}/\beta 2$ bound) and minimizing unbound Mn^{II}. With 75 μM Mn^{II}-loaded NrdF and 50 μM $NrdI_{hq}$ immediately after 1:1 mixing with O_2-saturated buffer, >97% of $NrdI_{hq}$ is complexed to NrdF. As noted above, 0.36 $Y^{\bullet}/\beta 2$ and 1.0 $Mn^{III}/\beta 2$ are produced (27 μM Mn^{III}_2-$Y^{\bullet}$, 11 μM Mn^{III}_2 not associated with $Y^{\bullet}$), whereas 2.2 $Mn^{II}/\beta 2$ is not oxidized. These yields are important in interpreting the kinetics results. The same conditions were used for both SF and RFQ-EPR analyses.

Given the number of absorbing species and the complexity of their spectra, in the initial SF experiments, the reaction was monitored between 310 and 700 nm in 10 nm increments, as well as at 405 and 415 nm (to better resolve the $Y^{\bullet}$). The spectra reconstructed from the individual SF traces are shown in Figure 4 in three time regimes for clarity. Based on these results, we carried out a more detailed analysis of the kinetic traces at 610, 340, and 410 nm (Figure S12). At 610 nm, $NrdI_{sq}$ formation and disappearance predominated, along with a small contribution (~5% of total amplitude) from Mn^{III}_2 cluster and $Y^{\bullet}$. Analysis at 340 nm allowed detection of a $Mn^{III}Mn^{IV}$ intermediate, and 410 nm was chosen as it is the λ_{max} of the $Y^{\bullet}$; all three oxidation states of NrdI also contribute at these two wavelengths. In the following sections these results are used to formulate the mechanistic proposal for Mn^{III}_2-$Y^{\bullet}$ cofactor assembly in Scheme 3 (all rate constants and amplitudes are in Table S3).

3.6.1. $NrdI_{sq}$ Production and Decay. The full spectrum analysis of the first time regime (83 ms) revealed $NrdI_{sq}$ formation at 610 nm and three isosbestic points, at 330, 390, and 415 nm, indicating direct conversion of $NrdI_{hq}$ to $NrdI_{sq}$ (Figure 4A). In the second and third regimes, $NrdI_{sq}$ decays by ~4 s to $NrdI_{ox}$, with an isosbestic point at ~500 nm. The plot of A_{610} (Figure 5, red trace, fit in black line), is fit best to four

dx.doi.org/10.1021/ja312457t | J. Am. Chem. Soc. 2013, 135, 4027−4039

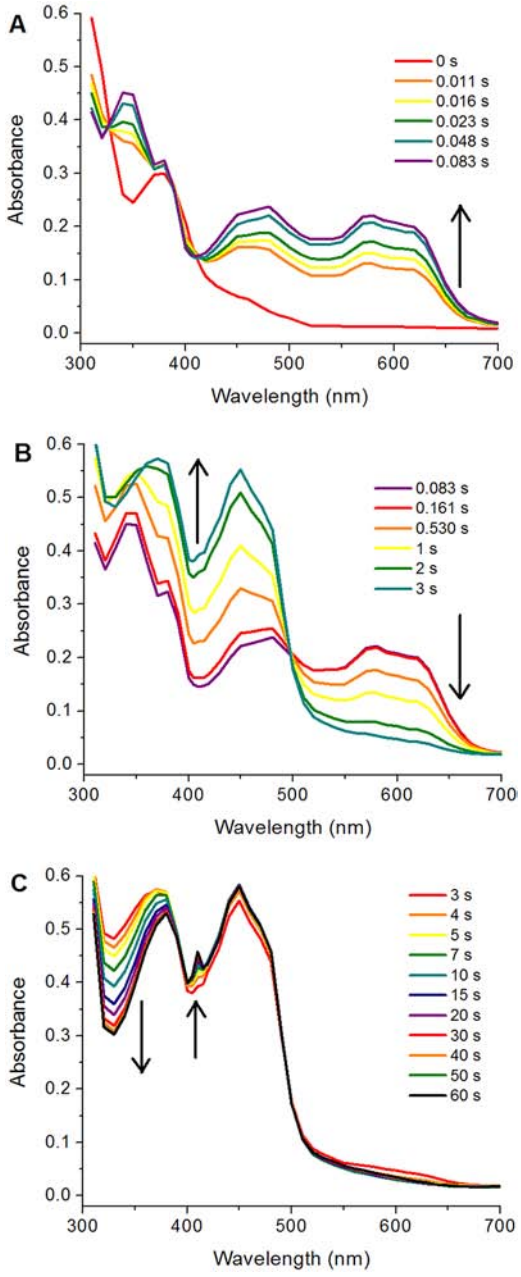

Figure 4. Reaction of 50 μM $NrdI_{hq}$ and 75 μM Mn^{II}-loaded NrdF with 0.6 mM O_2, as monitored by SF absorption spectroscopy, divided into three time regimes: 0–0.083 (A), 0.083–3 (B), and 3–60 s (C). The spectra are point-by-point reconstructions from kinetic traces acquired every 10 nm between 310 and 700 nm, as well as at 405 and 415 nm. One shot per wavelength is shown, but the data are representative of further experiments conducted at this and lower concentrations (10 μM $NrdI_{hq}$, 25 μM Mn^{II}_2-NrdF).

exponentials (Table 2, Figure S12A)—two increasing phases at 610 nm ($NrdI_{sq}$ formation), with rate constants of 40 s^{-1} (~75% of total NrdI) and 8 s^{-1} (~20%),[57] followed by a decreasing phase of 0.65 s^{-1} ($NrdI_{sq}$ oxidation to $NrdI_{ox}$), and finally a small increase of 0.15 s^{-1} (Mn^{III}_2 and $Y^\bullet$ formation, section 3.6.3).[58]

For comparison with the SF results, the reaction of $NrdI_{hq}$ with Mn^{II}-loaded NrdF and O_2 under identical conditions was monitored by the RFQ method (12 ms–60 s) and analyzed by EPR spectroscopy. $NrdI_{sq}$ can be quantified at 77 K, even in the presence of multiple Mn-derived signals and $Y^\bullet$, because its signal saturates at microwave powers orders of magnitude below the other paramagnetic species. The samples from 12 ms to 7 s were analyzed at 5 μW at 77 K and the results overlaid on the A_{610} trace of the SF reactions (Figure 5). The data show accumulation of 31 ± 5 μM sq at 83 ms—20% lower than the maximal accumulation of $NrdI_{sq}$ as determined from the SF trace at 610 nm (38 μM).

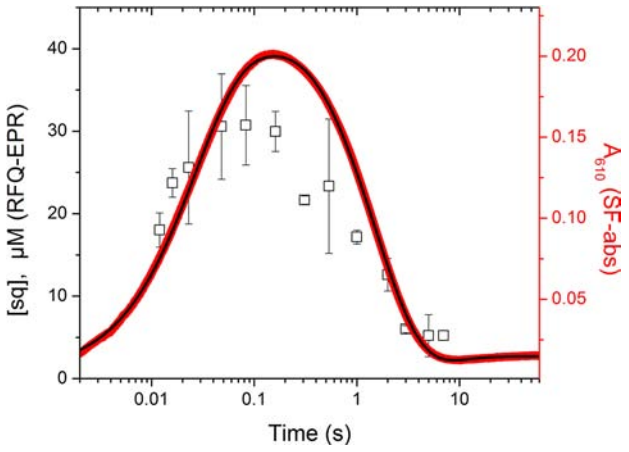

Figure 5. Formation and decay of $NrdI_{sq}$ in the reaction of $NrdI_{hq}$ and Mn^{II}-loaded NrdF with O_2, monitored by SF absorption and RFQ-EPR spectroscopies. $NrdI_{sq}$ was monitored by SF absorption spectroscopy at 610 nm (right axis, red line) and the trace fit to four exponentials (black line, Table 2). $NrdI_{sq}$ (left axis, black squares) was quantified by EPR spectroscopy (77 K, 5 μW) in RFQ time points quenched at the indicated times. Note that $NrdI_{sq}$ does not reach zero concentration due to a contribution from $Y^\bullet$ at >2 s time points, resulting in the smaller than expected amplitude for sq decay as determined by RFQ (Table 2). The two *y*-axes are scaled for direct comparison of the SF and RFQ-EPR data according to the extinction coefficient of $NrdI_{sq}$ at 610 nm, 4.9 ± 0.7 mM^{-1} cm^{-1}.[10].

Table 2. Apparent Rate Constants and Amplitudes for the Reaction of $NrdI_{hq}$ and Mn^{II}-Loaded NrdF with O_2, Determined by Fits to Single-Wavelength SF (610 nm) or RFQ-EPR (77 K) Data in Figure 5[a]

	SF, 610 nm			RFQ-EPR	
phase	k (s^{-1})	ΔA	amplitude (μM)	k (s^{-1})	amplitude (μM)[b]
sq formation (phase 1)	40	0.18	37	88 ± 38[c]	34 ± 16[c]
sq formation (phase 2)	8	0.05	10		
sq decay	0.65	−0.24	49	0.8 ± 0.2	27 ± 2
Mn^{III}_2-$Y^\bullet$ formation	0.15	0.012	27[d]		

[a]Values represent the data from 3 traces (SF) or 2–4 experiments (RFQ-EPR). Similar rate constants were obtained in SF studies at lower $NrdI_{hq}$ and NrdF concentrations (Figure S13 and Table 1). [b]Adjusted for packing factor. [c]The reaction is ~50% complete by the first time point, explaining the large uncertainty in these values (see text). [d]Mn^{III} not associated with $Y^\bullet$ is also produced in the assembly reaction. Assuming 27 μM Mn^{III}_2-$Y^\bullet$ and 11 μM Mn^{III}_2 (section 2.8.1) gives ΔA = 0.011, in good agreement with the observed ΔA.

The RFQ data can be fit to a two-exponential model with k_1 = 88 ± 38 s^{-1} and k_2 = 0.8 ± 0.2 s^{-1}. The larger than expected value of k_1 based on the SF data, and the large uncertainty in k_1 and its amplitude, reflect the observation that the $NrdI_{sq}$ formation reaction is 50% complete by the first time point

dx.doi.org/10.1021/ja312457t | J. Am. Chem. Soc. 2013, 135, 4027–4039

Table 3. Apparent Rate Constants and Amplitudes for $Mn^{III}Mn^{IV}$ Formation and Decay in the Reaction of $NrdI_{hq}$, Mn^{II}-Loaded NrdF, and O_2, Determined by Fits to Single-Wavelength SF (340 and 410 nm) or RFQ-EPR (10 or 77 K) Data[a]

	340 nm			410 nm			RFQ-EPR	
phase	k (s^{-1})	ΔA	amplitude (μM)	k (s^{-1})	ΔA	amplitude (μM)	k (s^{-1})	amplitude (μM)
$Mn^{III}Mn^{IV}$ formation	2.5	0.17	13 ± 4[b]	NA[c]	NA	NA	2.2 ± 0.4	19 ± 6[d]
$Mn^{III}Mn^{IV}$ decay	0.08	−0.16	19 ± 8[e]	0.09	0.054	25 ± 8[e]	0.12 ± 0.02	22 ± 7[d]

[a]Values represent the data from 3 traces (SF) or 2−4 experiments (RFQ-EPR). Similar rate constants were obtained in SF studies at lower $NrdI_{hq}$ and NrdF concentrations (Figure S13). [b]For phases involving $Mn^{III}Mn^{IV}$ formation or decay, we have assumed ε_{340} = 13 ± 4 mM^{-1} cm^{-1} and ε_{410} = 3 ± 1 mM^{-1} cm^{-1}. These values were determined from Figure S14 on the basis of the estimated UV−vis spectrum of the intermediate and the quantification of the EPR spectrum of $Mn^{III}Mn^{IV}$ by simulation at 3 time points (section 2.9). [c]NA: not applicable (not observable at this wavelength). Given that the $Mn^{III}Mn^{IV}$ intermediate should contribute ∼+0.07 to ΔA_{410} (Figure S14), it is probable that this phase was not resolved from that of sq decay in the fits because its rate constant for formation is somewhat similar to that for sq decay, and of the same sign (see Table S3). [d]Uncertainty includes uncertainties in fit and in concentration of $Mn^{III}Mn^{IV}$ (∼30%) [e]Concentrations of Mn^{III}_2-Y• (27 μM) and Mn^{III}_2 (11 μM) are taken as given (section 2.8.1)

(Figure 5).[59] k_2 agrees well with the rate constant for sq decay determined by SF absorption (Scheme 3). Thus, the SF and RFQ-EPR data are in agreement that ∼60−70% $NrdI_{hq}$ reacts with O_2 at ∼40−60 s^{-1} to form $NrdI_{sq}$ and $O_2^{\bullet-}$.[60] This rate constant is ∼5 times faster than that of the major phase of $NrdI_{sq}$ formation in the presence of apoNrdF (7.4 s^{-1}) and ∼40 times faster than the rate constant for $NrdI_{sq}$ formation in the absence of NrdF (1.6 mM^{-1} s^{-1}; 1 s^{-1} at 0.6 mM O_2).

3.6.2. Formation and Decay of a $Mn^{III}Mn^{IV}$ Intermediate. The reconstructed spectra in Figure 4B in the 83 ms−3 s regime are dominated in the visible region by the conversion of $NrdI_{sq}$ to $NrdI_{ox}$, with an isosbestic point at ∼500 nm. Absence of the $NrdI_{sq}/NrdI_{ox}$ isosbestic point at ∼350 nm (Figure 1A) indicates formation of an additional, UV-absorbing species; the 300−350 nm region displays significantly higher absorbance than can be attributed to $NrdI_{ox}$ (Figure 1A). This absorbance is more clearly observed in the spectra from the 3−60 s regime, in which features in the 300−350 nm region decay as the sharp feature of the Y• grows in at 410 nm (arrows, Figure 4C). The A_{340} SF traces (Figure S12B, Table 3) suggest formation and decay of this UV absorbing feature at 2.5 and 0.08 s^{-1}, respectively.

The UV−vis spectrum of this species was estimated from the spectrum of the 2 s time point reconstructed from the SF data. At this time point, substantial intermediate is present, little Y• is apparent (Figure 4B), and NrdI is entirely in the sq and ox forms. After subtraction of the contributions of $NrdI_{sq}$ (13 μM, Figure 5), $NrdI_{ox}$ (37 μM), and protein scattering, the relatively featureless spectrum with little visible absorption shown in Figure S14 was obtained. This spectrum is similar to that of the $Mn^{III}Mn^{IV}$ form of Mn catalase[61] and synthetic models.[62]

The identity of the intermediate was determined by analysis of the RFQ samples at 10 K, where possible EPR-active intermediates in cofactor formation ($Mn^{II}Mn^{III}$ and $Mn^{III}Mn^{IV}$) may be observable. A spectral component that has 16 resonance lines is present in the X-band EPR data of RFQ reaction intermediates trapped between 12 ms and 30 s (Figure S15). These features are very similar to those of strongly exchange-coupled $Mn^{III}Mn^{IV}$ dimers.[63] Indeed, the best fit of this contribution to the 2 s spectrum (obtained after subtraction of a scaled spectrum of the starting material to remove the contribution from unreacted Mn^{II}-loaded NrdF) requires two ^{55}Mn ions with effective HFIs of [−465 −435 −310] and [230 230 240] MHz for the Mn^{III} and Mn^{IV} centers, respectively (Figure 6, section S2.5). These values are nearly identical to those determined for the superoxidized form of Mn catalase.[63] Importantly, there is no spectroscopic evidence for the presence of a $Mn^{II}Mn^{III}$ form of the cluster at any point in the reaction. Owing to the large intrinsic HFI for Mn^{II} centers as well as the larger projection factors, the EPR spectrum of an antiferromagnetically coupled $Mn^{II}Mn^{III}$ dimer is expected to be spread over a much larger field range than that typically observed for a $Mn^{III}Mn^{IV}$ dimer.[63]

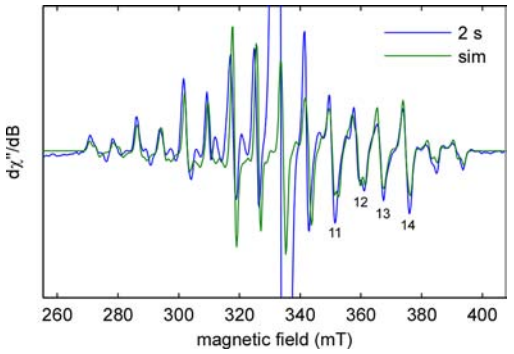

Figure 6. Simulation of the EPR spectrum of the $Mn^{III}Mn^{IV}$ intermediate. The spectrum was obtained by subtraction of a scaled spectrum of the Mn^{II}-loaded NrdF starting material from the spectrum of the RFQ mixture of 75 μM NrdF, 50 μM NrdI, and oxygenated buffer after 2 s aging time. Simulation of the spectrum was performed as described (section 2.9). Peaks 11−14 are labeled. Spectrometer settings: temperature = 10 K; microwave frequency = 9.38 GHz; power = 20 μW; modulation amplitude = 0.5 mT; modulation frequency = 100 kHz; sweep rate = 5.3 mT/s. The off-scale feature at ∼330 mT is due to $NrdI_{sq}$.

For the lowest field feature of the $Mn^{III}Mn^{IV}$ multiline signal, there is a noticeable shift upfield from 270.1 to 271.3 mT as the reaction progresses (see Figure S15). Additional changes in spectral line shape are also observed for the highest field features. These small perturbations of the effective ^{55}Mn HFI likely result from changes in either the exchange coupling parameter J, or in the Mn^{III} zero-field splitting constant, possibly due to a change in protonation state of a bridging oxo group or a solvent-derived ligand to the Mn^{III} ion, respectively.

In order to quantify the $Mn^{III}Mn^{IV}$ intermediate and determine its rates of formation and decay, we first used the intensity of peak 14 at ∼373 mT (Figure 6) to estimate the relative concentrations of the $Mn^{III}Mn^{IV}$ species at each time point. The results of this analysis are plotted in Figure 7, fit to rate constants of 2.2 ± 0.4 and 0.12 ± 0.02 s^{-1}. The similarity of these rate constants to those from the SF analysis strongly suggests that the UV-absorbing intermediate and the EPR-active $Mn^{III}Mn^{IV}$ are the same species. Interestingly, the rate

dx.doi.org/10.1021/ja312457t | J. Am. Chem. Soc. 2013, 135, 4027−4039

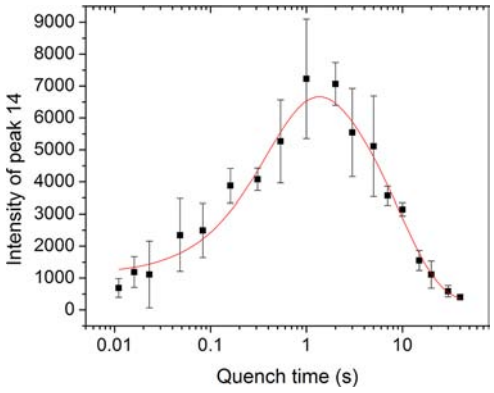

Figure 7. Concentration of the $Mn^{III}Mn^{IV}$ intermediate, followed by the peak-to-trough intensity of peak 14 (Figure 6). The data (black, mean ± SD for 2−4 independent experiments) are fitted to a two-phase model (red) with rate constants given in Table 3.

constant for formation of $Mn^{III}Mn^{IV}$ is 20 times slower than the rate of $NrdI_{sq}$ generation (section 4.3).

The relative concentrations of the intermediate were then converted to absolute concentrations (Figure S16) by determination of a scaling factor between the peak intensities in Figure 7 and the concentrations of $Mn^{III}Mn^{IV}$ obtained by quantitative simulations (30% uncertainty) of three of the RFQ samples (section 2.9). The presence of multiple paramagnetic species in the reaction mixture—Mn^{II}_2-NrdF, Mn^{II}, $NrdI_{sq}$, and $Y^\bullet$—requires that, before simulation of $Mn^{III}Mn^{IV}$, the contribution from unreacted Mn^{II}-loaded NrdF be subtracted from the spectra using the broad features centered at ∼290 and 410 mT, outside the envelope of Mn^{II}, $Y^\bullet$, and $NrdI_{sq}$ (Figure 2A). As shown in Table 3 and Figure S16, the maximal concentration of $Mn^{III}Mn^{IV}$ estimated by this method was 19 ± 8 μM, at ∼1.5 s. While $Mn^{III}Mn^{IV}$ could, in principle, be on pathway to form Mn^{III}_2-$Y^\bullet$, Mn^{III}_2 cluster, or both, the 19 ± 8 μM value most likely underestimates the amount of $Mn^{III}Mn^{IV}$ formed, as the RFQ-EPR result underestimated the concentration of $NrdI_{sq}$ by 20% (Figure 5). This is consistent with the intermediate being a precursor to the 27 μM Mn^{III}_2-$Y^\bullet$ cofactor formed under these conditions. This conclusion is supported by the kinetics of $Y^\bullet$ formation, as described below.

In an effort to facilitate characterization and quantification of the $Mn^{III}Mn^{IV}$ species, we also generated the Y105F mutant of *B. subtilis* NrdF (sections S1.3 and S2.6). This mutant bound Mn^{II} more tightly than wt NrdF did (Figure S17), but little fluorescence change was observed in titrations to determine $NrdI_{hq}$/Y105F-NrdF affinity, indicating that $NrdI_{hq}$ bound Mn^{II}_2-Y105F NrdF either weakly or incorrectly (Figure S18). SF studies monitoring reaction of $NrdI_{hq}$ and Mn^{II}_2-Y105F NrdF with O_2 revealed no evidence of a $Mn^{III}Mn^{IV}$ intermediate (Figure S19).

3.6.3. $Y^\bullet$ Generation. To determine the kinetics of $Y^\bullet$ generation and whether the $Mn^{III}Mn^{IV}$ intermediate is kinetically competent for its formation, the single wavelength trace at 410 nm, the λ_{max} of the $Y^\bullet$, was fit to three exponentials (Figure S12C, Table 3, Table S3). The fastest phase, a small decrease at 48 s^{-1}, is attributed to the oxidation of $NrdI_{hq}$ to $NrdI_{sq}$ (ε_{410} values of these species differ by only 0.35 mM^{-1} cm^{-1}, Figure 1A). The second and major phase is an increase with k = 0.74 s^{-1} and an amplitude consistent with oxidation of $NrdI_{sq}$ to $NrdI_{ox}$. The slowest phase (k = 0.09 s^{-1}) is associated with the appearance of the sharp feature of $Y^\bullet$ (Figure 4C). The observed amplitude of this phase is consistent with decay of 25 ± 8 μM $Mn^{III}Mn^{IV}$ (Table 3). Because $NrdI_{sq}$ and/or $Mn^{III}Mn^{IV}$ contribute significantly to the 77 K EPR spectra of all but the 30, 40, and 60 s RFQ samples, independent determination of the rate constant for $Y^\bullet$ formation by EPR spectroscopy is problematic. However, the rate constants for $Mn^{III}Mn^{IV}$ decay by RFQ-EPR (0.12 ± 0.02 s^{-1}) and SF (0.09−0.15 s^{-1} at 340 and 610 nm) and $Y^\bullet$ formation by SF (0.08 s^{-1} at 410 nm) are in agreement (Table 3). Therefore, despite the somewhat lower than expected maximal concentration of $Mn^{III}Mn^{IV}$ determined by simulation of the RFQ-EPR data, the kinetic results together strongly suggest that the $Mn^{III}Mn^{IV}$ intermediate is responsible for oxidation of tyrosine to $Y^\bullet$.

3.6.4. Interpretation of the Rate Constant for $NrdI_{sq}$ Decay. In all rapid kinetics experiments, regardless of the presence/absence of NrdF and as long as SOD is present, the rate constant for reaction of $NrdI_{sq}$ with O_2 (eq 2) is ∼1 s^{-1} (Table 2). This rate constant is lower than that for $Mn^{III}Mn^{IV}$ formation (2.2 ± 0.4 s^{-1}), which suggests that the $O_2^{\bullet-}$ produced by $NrdI_{sq}$ oxidation is not involved in $Mn^{III}Mn^{IV}$ generation and that $O_2^{\bullet-}$ generated by $NrdI_{hq}$ oxidation is predominantly responsible for Mn^{II}_2 oxidation. Furthermore, the observation that the rate of $NrdI_{sq}$ oxidation is not accelerated in the presence of Mn^{II}-loaded NrdF also suggests that no further reducing equivalents, such as those required to reduce a tryptophan radical,[20,21] are needed for cluster assembly. Thus, $O_2^{\bullet-}$ provides the three oxidizing equivalents required for Mn^{III}_2-$Y^\bullet$ cofactor generation.

4. DISCUSSION

4.1. Kinetic Complexity in Mn^{III}_2-$Y^\bullet$ Cofactor Assembly. Together, the SF and EPR results described in this article strongly support the mechanistic model of Mn^{III}_2-$Y^\bullet$ cofactor assembly in Scheme 3. Following a treatment of several of the complexities that have been encountered in the course of the analysis, we discuss each reaction in Scheme 3 in turn.

Interestingly, 31−37 μM $NrdI_{sq}$ is generated in the fastest phase of the cluster assembly reaction, in conditions that give 27 μM $Y^\bullet$ and 75 μM Mn oxidized. Thus ∼2 Mn^{II} are oxidized for every $O_2^{\bullet-}$ produced in the fast phase, which may suggest that all of the Mn oxidized is present in dinuclear Mn^{III}_2 clusters. It is not clear why $Y^\bullet$ is generated in only ∼70% of these clusters—but the analogous question in class Ia diferric-$Y^\bullet$ assembly, in which only 1.2 $Y^\bullet$/β2 are generated despite oxidation of 3.6 Fe/β2, is also unanswered despite 20 years of mechanistic study.

The formation of substoichiometric levels of $NrdI_{sq}$ could be related to heterogeneity in NrdF due to incomplete/incorrect Mn^{II} binding or to NrdI's ability to react with O_2 by two pathways (eqs 1−3). Approximately 70% of $NrdI_{hq}$ reacts with O_2 to form $NrdI_{sq}$ in the absence or presence of Mn^{II}-loaded NrdF, suggesting that the complexity may be the result of using NrdI stoichiometrically, whereas it likely acts catalytically in vivo based on the reported amounts of NrdI and NrdF in *B. subtilis* and *E. coli*.[9,10] In vivo, $NrdI_{hq}$ can be rapidly regenerated by a NrdI reductase. This reductase has not been identified, but NrdI's role as a one-electron donor suggests that the reductant is likely flavodoxin (ferredoxin) reductase. A flavodoxin reductase has yet to be identified in *B. subtilis*. Interaction with the reductase may also influence the reaction of $NrdI_{hq}$ with O_2 to favor $O_2^{\bullet-}$ production.

dx.doi.org/10.1021/ja312457t | J. Am. Chem. Soc. 2013, 135, 4027−4039

4.2. Reaction of $NrdI_{hq}$ with O_2. The rate acceleration of $NrdI_{hq}$ oxidation in the presence of NrdF and O_2 may be caused by positively charged residues we have previously noted on NrdF at the NrdI binding site (R196 and K27 in *B. subtilis* NrdF).[23,50] Positively charged groups in the vicinity of the reactive C4a position of the flavin, thought to facilitate formation of the sq-$O_2^{\bullet-}$ pair, are key features of the active sites of many flavoproteins that react with O_2 as part of their catalytic cycles.[64] Our observed rate constants for reaction of $NrdI_{hq}$ with O_2 in the presence of NrdF to form $O_2^{\bullet-}$ are comparable to the rate constants for reaction of many flavoprotein oxidases with O_2.[64]

The reaction of $NrdI_{sq}$ with O_2 in *B. subtilis* NrdI (0.65−0.8 s^{-1}, 0.6 mM O_2) is nearly 2 orders of magnitude slower than the reaction of the hq and insensitive to the presence of NrdF. The hq and neutral sq forms of NrdI (and flavodoxins in general) are protonated at the N5 position of the flavin, whereas the ox form is deprotonated at this position. Crystal structures of flavodoxins[65] and NrdIs[23,38,66] have revealed that a peptide loop region (the "40s loop" in *B. subtilis*) in the vicinity of C4a undergoes a conformational change upon flavin reduction to allow a hydrogen bond between N5H and a peptide backbone carbonyl. The proton transfer and accompanying conformational change are reasonable sources of a kinetic barrier to sq oxidation (e.g., ref 67). This hypothesis is supported by the decrease in the rate constant for sq decay with decreasing pH (Table S1). The observation that the rate constant for $NrdI_{sq}$ oxidation is not significantly changed in the presence of NrdF indicates either that the conformational change and proton transfer are rate limiting even if $NrdI_{sq}$ is bound to NrdF, or that $NrdI_{sq}$ dissociates from NrdF before reacting with O_2. Further studies are required to determine when in the course of the cluster assembly reaction NrdI dissociates from NrdF, as sq or ox.

4.3. Formation of the $Mn^{III}Mn^{IV}$ Intermediate. Having identified $O_2^{\bullet-}$ as the oxidant in our current studies, we suggest that $O_2^{\bullet-}$ oxidizes the Mn^{II}_2 cluster by inner- or outer-sphere electron transfer, possibly coupled with proton transfer. It is also possible that superoxide binds to the metal site in the protonated form, $HO_2^{\bullet}$ (pK_a = 4.9), analogous to the case of azide binding to hemerythrin, in which HN_3 (pK_a = 4.75) is proposed to be the species that binds to the metal site.[68] From our biochemical[7] and crystallographic[23] data on the *E. coli* class Ib system, we proposed that the oxidant channels from NrdI to the metal site via a hydrophilic tunnel within the NrdI·NrdF complex. The orientation of the channel suggests that $(H)O_2^{\bullet}$ would first encounter Mn2, the Mn^{II} site farthest from Y105.[23,50] Therefore, we propose initial formation of a $Mn^{II}Mn^{III}$ intermediate or $Mn^{II}Mn^{III}$−OO(H) adduct, with Mn^{III} being at site 2. To cleave the O−O bond and generate a $Mn^{III}Mn^{IV}$ intermediate similar to superoxidized Mn catalase (μ-oxo, μ-hydroxo bridged),[63,69] a (hydro)peroxo-bridged $Mn^{II}Mn^{III}$ species, possibly analogous to the μ-1,2-peroxodiferric intermediate proposed in class Ia RNR Fe^{III}_2-$Y^{\bullet}$ cofactor assembly (Scheme 1),[13] may be formed at least transiently.

A $Mn^{II}Mn^{III}$ species that forms and accumulates should be detectable by UV−vis absorption and EPR spectroscopies. The UV−vis spectrum of the $Mn^{II}Mn^{III}$ would be expected to be similar to that of the Mn^{III}_2 cluster (Figure 1B) but with half the extinction coefficient; the weak absorption features would be difficult to detect in our SF absorption experiments, overwhelmed by the flavin absorption bands. We see no evidence of a coupled $Mn^{II}Mn^{III}$ intermediate from our RFQ-EPR analysis. Because of the presence of free Mn^{II} in the starting material, we cannot rule out the possibility of an uncoupled $Mn^{II}Mn^{III}$ species, which would give rise to a signal resembling mononuclear Mn^{II}. However, there is a long window as $Mn^{III}Mn^{IV}$ is formed an order of magnitude more slowly than the fast, major phase of $NrdI_{sq}$ generation. If the oxidation of the site 2 Mn^{II} to generate a $Mn^{II}Mn^{III}$ intermediate occurs and is similar to the analogous reaction in SOD, it is expected to be very fast (10^9 M^{-1} s^{-1} for Mn^{II}-SOD[70]). One explanation for our inability to detect this type of intermediate is that all steps between $O_2^{\bullet-}$ production and $Mn^{III}Mn^{IV}$ formation may be rate-limited by a conformational change associated with the $O_2^{\bullet-}$ reaching the metal site. Based on crystal structures of Mn^{II}_2-, Fe^{II}_2-, Mn^{III}_2-, and Fe^{III}_2-NrdFs, and of the *E. coli* Mn^{II}_2-NrdF·$NrdI_{hq}$ complex, we propose that this conformational change may be a reorganization of the αE helix of NrdF (Figure S20). This helix contains three completely conserved residues that undergo rearrangements accompanying oxidation of the metal site—two residues near the metal site (F162/168 and E158/164, *E. coli*/*B. subtilis* numbering), the latter being a ligand to Mn2, and one residue in the oxidant channel (Y163/Y169) that also forms part of the NrdI binding site. Movement of this helix connecting the metal site, channel, and NrdI binding site could ensure both that NrdI remains bound while $O_2^{\bullet-}$ is in the channel and that NrdI dissociates once $O_2^{\bullet-}$ reaches the metal site.

In our model, an important consequence of $O_2^{\bullet-}$ encountering and reacting with Mn2 initially is that the Mn^{IV} is at site 2 (Scheme 3), where the Fe^{IV} is proposed to reside in intermediate **X**,[71] providing a close analogy between the tyrosine-oxidizing intermediates in Fe^{III}_2-$Y^{\bullet}$ and Mn^{III}_2-$Y^{\bullet}$ cluster assembly in class Ia and Ib RNRs. In addition, an analogy can be drawn to the formation of a $Mn^{IV}Fe^{III}$ cofactor in the class Ic RNR from *Chlamydia trachomatis*, in which the $Y^{\bullet}$-forming tyrosine is replaced by phenylalanine.[72] In the class Ic RNR, a $Mn^{II}Fe^{II}$ cluster reacts with O_2 to generate a $Mn^{IV}Fe^{IV}$ intermediate, which decays slowly to the active $Mn^{IV}Fe^{III}$ cofactor.[73] Recent studies suggest that Mn occupies site 1 and Fe site 2 in this cofactor.[74,75] Thus, despite using different metallocofactors, all three class I RNRs have engineered their metal sites such that the site 2 metal is reduced by one electron in the conversion between the final intermediate and the active cofactor.

4.4. Tyrosine Oxidation. The kinetic data indicate that $Mn^{III}Mn^{IV}$ decays concomitant with $Y^{\bullet}$ generation, suggesting that it is the oxidant directly responsible for tyrosine oxidation. This reaction is notable for its slow rate constant: 0.1 s^{-1} (25 °C), compared to 1 and 5 s^{-1} (both at 5 °C) for oxidation of tyrosine by **X** in *E. coli* and mouse class Ia RNRs, respectively.[15,76] Although it is not known whether electron, proton, or coupled electron/proton transfer is rate-limiting for tyrosine oxidation in these systems, the very slow oxidation of tyrosine to $Y^{\bullet}$ by a $Mn^{III}Mn^{IV}$ intermediate may reflect its lower reduction potential compared to **X**, as has been suggested on the basis of calculations on other RNR systems.[77]

5. CONCLUDING REMARKS

Comparison of the general mechanisms of Mn^{III}_2-$Y^{\bullet}$ and Fe^{III}_2-$Y^{\bullet}$ cofactor assembly (Schemes 1 and 3) demonstrates Nature's elegant and efficient strategy to balance two inherent problems in enzymatic $Y^{\bullet}$ generation: activation of O_2 and the need for an odd number of electrons for $Y^{\bullet}$ generation. In Fe^{III}_2-$Y^{\bullet}$ cofactor assembly, reaction of O_2 with a Fe^{II}_2 center is facile,

dx.doi.org/10.1021/ja312457t | J. Am. Chem. Soc. 2013, 135, 4027−4039

but an extra electron is delivered *after* O_2 activation to form the stable Fe^{III}_2-$Y^{\bullet}$ cofactor. To our knowledge, only one biological Mn^{II} center has been suggested to be transiently oxidized by O_2 at a physiologically relevant rate,[78] and it does so with the help of an electron-donating cosubstrate. In NrdF, the most efficient strategy for circumventing this problem is to deliver the extra electron as the *first* step in the process in the form of $O_2^{\bullet-}$, with which Mn^{II} reacts readily. Reduction of O_2 requires $NrdI_{hq}$; efforts to assemble Mn^{III}_2-$Y^{\bullet}$ using exogenous $O_2^{\bullet-}$ have been unsuccessful (section S2.7). Once $O_2^{\bullet-}$ is generated, the three oxidizing equivalents necessary for formation of the $Mn^{III}Mn^{IV}$ intermediate and, subsequently, a $Y^{\bullet}$ are present. This is a more economical mechanism than use of H_2O_2 as oxidant, which would require 2 O_2 and 5 added reducing equivalents to form one $Y^{\bullet}$ (Scheme 2).

An important question stemming from these results is how class Ib RNRs assemble both Mn^{III}_2-$Y^{\bullet}$ and Fe^{III}_2-$Y^{\bullet}$ cofactors, whereas class Ia RNRs assemble only Fe^{III}_2-$Y^{\bullet}$ cofactors. The structural[50] and mechanistic similarities between these systems suggest that the most incisive answer to this question may not be found at the metal site, but instead in the ways in which the unique difficulties of $O_2^{\bullet-}$ production and transport to the metal site have been solved for cluster formation in class Ib RNRs. Production of $O_2^{\bullet-}$ requires a specific accessory protein, NrdI. The oxidant channels[23] in class Ib RNRs appear configured for transport of a hydrophilic molecule like $O_2^{\bullet-}$, distinct from the proposed O_2 access route to the diferrous site in the class Ia RNRs, which is largely hydrophobic.[79,80] Thus Mn^{III}_2-$Y^{\bullet}$ cofactor assembly in the class Ib RNRs represents a remarkable example of how Nature has expanded the range of chemistry that can be performed by the dimetal–carboxylate structural motif, by creating and harnessing a normally deleterious oxidant for an essential cellular purpose.

■ ASSOCIATED CONTENT

Supporting Information

Experimental details of the determination of the UV–vis spectra of the Mn^{III}_2 cluster and $Y^{\bullet}$; NrdI-NrdF K_d determination; expression, purification, and characterization of Y105F NrdF; EPR simulations; and attempts at cluster assembly using KO_2; as well as eqs S1–S9, Tables S1–S3, and Figures S1–S20. This material is available free of charge via the Internet at http://pubs.acs.org.

■ AUTHOR INFORMATION

Corresponding Author

stubbe@mit.edu; rdbritt@ucdavis.edu

Present Address

[⊥]Department of Chemistry, University of California, Berkeley, CA 94720

Notes

The authors declare no competing financial interest.

■ ACKNOWLEDGMENTS

The work in the Stubbe laboratory was supported by National Institutes of Health Grant GM81393 to J.S. and a National Defense Science and Engineering Graduate Fellowship to J.A.C. The Mn EPR work in the Britt laboratory was funded by the Division of Chemical Sciences, Geosciences, and Biosciences, Office of Basic Energy Sciences of the U.S. Department of Energy through Grant DESC0007203 to R.D.B. We thank S. J. Lippard for use of his laboratory's AA spectrometer, A.-F. Miller for helpful discussions related to the use of potassium superoxide in cluster assembly, and B. A. Palfey for a critical reading of a previous version of this manuscript. We are also grateful to A. K. Boal, who proposed the structural basis for the conformational change suggested to rate-limit $Mn^{III}Mn^{IV}$ formation and who made Figure S20 to illustrate it.

■ REFERENCES

(1) Nordlund, P.; Reichard, P. *Annu. Rev. Biochem.* **2006**, *75*, 681–706.
(2) Cotruvo, J. A., Jr.; Stubbe, J. *Annu. Rev. Biochem.* **2011**, *80*, 733–767.
(3) Licht, S.; Gerfen, G. J.; Stubbe, J. *Science* **1996**, *271*, 477–481.
(4) Licht, S.; Stubbe, J. In *Comprehensive Natural Products Chemistry*; Poulter, C. D., Ed.; Elsevier Science: New York, 1999; Vol. *5*, p 163–203.
(5) Atkin, C. L.; Thelander, L.; Reichard, P.; Lang, G. *J. Biol. Chem.* **1973**, *248*, 7464–7472.
(6) Ehrenberg, A.; Reichard, P. *J. Biol. Chem.* **1972**, *247*, 3485–3488.
(7) Cotruvo, J. A., Jr.; Stubbe, J. *Biochemistry* **2010**, *49*, 1297–1309.
(8) Cox, N.; Ogata, H.; Stolle, P.; Reijerse, E.; Auling, G.; Lubitz, W. *J. Am. Chem. Soc.* **2010**, *132*, 11197–11213.
(9) Cotruvo, J. A., Jr.; Stubbe, J. *Biochemistry* **2011**, *50*, 1672–1681.
(10) Zhang, Y.; Stubbe, J. *Biochemistry* **2011**, *50*, 5615–5623.
(11) Huque, Y.; Fieschi, F.; Torrents, E.; Gibert, I.; Eliasson, R.; Reichard, P.; Sahlin, M.; Sjöberg, B. M. *J. Biol. Chem.* **2000**, *275*, 25365–25371.
(12) Stubbe, J.; Riggs-Gelasco, P. *Trends Biochem. Sci.* **1998**, *23*, 438–443.
(13) Yun, D.; Garcia-Serres, R.; Chicalese, B. M.; An, Y. H.; Huynh, B. H.; Bollinger, J. M., Jr. *Biochemistry* **2007**, *46*, 1925–1932.
(14) Tong, W. H.; Chen, S.; Lloyd, S. G.; Edmondson, D. E.; Huynh, B. H.; Stubbe, J. *J. Am. Chem. Soc.* **1996**, *118*, 2107–2108.
(15) Bollinger, J. M., Jr.; Edmondson, D. E.; Huynh, B. H.; Filley, J.; Norton, J. R.; Stubbe, J. *Science* **1991**, *253*, 292–298.
(16) Ravi, N.; Bollinger, J. M., Jr.; Huynh, B. H.; Edmondson, D. E.; Stubbe, J. *J. Am. Chem. Soc.* **1994**, *116*, 8007–8014.
(17) Bollinger, J. M., Jr.; Tong, W. H.; Ravi, N.; Huynh, B. H.; Edmondson, D. E.; Stubbe, J. *J. Am. Chem. Soc.* **1994**, *116*, 8015–8023.
(18) Sturgeon, B. E.; Burdi, D.; Chen, S.; Huynh, B. H.; Edmondson, D. E.; Stubbe, J.; Hoffman, B. M. *J. Am. Chem. Soc.* **1996**, *118*, 7551–7557.
(19) Shanmugam, M.; Doan, P. E.; Lees, N. S.; Stubbe, J.; Hoffman, B. M. *J. Am. Chem. Soc.* **2009**, *131*, 3370–3376.
(20) Bollinger, J. M., Jr.; Tong, W. H.; Ravi, N.; Huynh, B. H.; Edmondson, D. E.; Stubbe, J. *J. Am. Chem. Soc.* **1994**, *116*, 8024–8032.
(21) Baldwin, J.; Krebs, C.; Ley, B. A.; Edmondson, D. E.; Huynh, B. H.; Bollinger, J. M., Jr. *J. Am. Chem. Soc.* **2000**, *122*, 12195–12206.
(22) Wu, C.-H.; Jiang, W.; Krebs, C.; Stubbe, J. *Biochemistry* **2007**, *46*, 11577–11588.
(23) Boal, A. K.; Cotruvo, J. A., Jr.; Stubbe, J.; Rosenzweig, A. C. *Science* **2010**, *329*, 1526–1530.
(24) Fish, W. W. *Methods Enzymol.* **1988**, *158*, 357–364.
(25) Parkin, S. E.; Chen, S.; Ley, B. A.; Mangravite, L.; Edmondson, D. E.; Huynh, B. H.; Bollinger, J. M., Jr. *Biochemistry* **1998**, *37*, 1124–1130.
(26) Cotruvo, J. A., Jr.; Stubbe, J. *Proc. Natl. Acad. Sci. U.S.A.* **2008**, *105*, 14383–14388.
(27) Mayhew, S. G.; Massey, V. *J. Biol. Chem.* **1969**, *244*, 794–802.
(28) Wilhelm, E.; Battino, R.; Wilcock, R. J. *Chem. Rev.* **1977**, *77*, 219–262.
(29) Eftink, M. R. *Methods Enzymol.* **1997**, *278*, 221–257.
(30) Johnson, K. A.; Simpson, Z. B.; Blom, T. *Anal. Biochem.* **2009**, *387*, 20–29.
(31) Johnson, K. A.; Simpson, Z. B.; Blom, T. *Anal. Biochem.* **2009**, *387*, 30–41.

(32) These concentrations were chosen to simplify the kinetics of NrdI oxidation, rather than to maximize Y• yield (0.6 Y•/β2); see section 3.6.
(33) Ballou, D. P. *Methods Enzymol.* **1978**, *54*, 85−93.
(34) Bollinger, J. M., Jr.; Tong, W. H.; Ravi, N.; Huynh, B. H.; Edmondson, D.; Stubbe, J. *Methods Enzymol.* **1995**, *258*, 278−303.
(35) Ballou, D. P.; Palmer, G. A. *Anal. Chem.* **1974**, *46*, 1248−1253.
(36) Malmström, B. G.; Reinhammar, B.; Vanngard, T. *Biochim. Biophys. Acta* **1970**, *205*, 48−57.
(37) Stoll, S.; Schweiger, A. *J. Magn. Reson.* **2006**, *178*, 42−55.
(38) Røhr, Å. K.; Hersleth, H.-P.; Andersson, K. K. *Angew. Chem., Int. Ed.* **2010**, *49*, 2324−2327.
(39) Whittaker, M. M.; Barynin, V. V.; Antonyuk, S. V.; Whittaker, J. W. *Biochemistry* **1999**, *38*, 9126−9136.
(40) Whittaker, J. W.; Whittaker, M. M. *J. Am. Chem. Soc.* **1991**, *113*, 5528−5540.
(41) Whittaker, M. M.; Barynin, V. V.; Igarashi, T.; Whittaker, J. W. *Eur. J. Biochem.* **2003**, *270*, 1102−1116.
(42) Palmer, G.; Müller, F.; Massey, V. In *Flavins and Flavoproteins: Proceedings of the Third International Symposium on Flavins and Flavoproteins*; Kamin, H., Ed.; University Press: Baltimore, 1971; pp 123−140.
(43) Epel, B.; Schäfer, K.-O.; Quentmeier, A.; Friedrich, C.; Lubitz, W. *J. Biol. Inorg. Chem.* **2005**, *10*, 636−642.
(44) Golombeck, A. P.; Hendrich, M. P. *J. Magn. Reson.* **2003**, *165*, 33−48.
(45) Fielding, L.; More, K. M.; Eaton, G. R.; Eaton, S. S. *J. Am. Chem. Soc.* **1986**, *108*, 8194−8196.
(46) Szalai, V. A.; Kuehne, H.; Lakshmi, K. V.; Brudvig, G. W. *Biochemistry* **1998**, *37*, 13594−13603.
(47) Tomter, A. B.; Zoppellaro, G.; Andersen, N. H.; Hersleth, H.-P.; Hammerstad, M.; Røhr, Å. K.; Sandvik, G. K.; Strand, K. R.; Nilsson, G. E.; Bell, C. B., III; Barra, A.-L.; Blasco, E.; LePape, L.; Solomon, E. I.; Andersson, K. K. *Coord. Chem. Rev.* **2013**, *257*, 3−26.
(48) Θ corresponds to the dihedral angle between a vector that is normal to the phenoxyl plane and the β1 proton. The β2 proton is assumed to have a dihedral angle equal to 120° − Θ.
(49) Svistunenko, D. A.; Cooper, C. E. *Biophys. J.* **2004**, *87*, 582−595.
(50) Boal, A. K.; Cotruvo, J. A., Jr.; Stubbe, J.; Rosenzweig, A. C. *Biochemistry* **2012**, *51*, 3861−3871.
(51) Ghisla, S.; Massey, V.; Lhoste, J.-M.; Mayhew, S. G. *Biochemistry* **1974**, *13*, 589−597.
(52) The extinction coefficient was calculated using ExPASy (see ref 10). However, stoichiometries of metal binding are generally ∼3.5 per dimer in β2 subunits purified to date.
(53) Crona, M.; Torrents, E.; Røhr, Å. K.; Hofer, A.; Furrer, E.; Tomter, A. B.; Andersson, K. K.; Sahlin, M.; Sjöberg, B. M. *J. Biol. Chem.* **2011**, *286*, 33053−33060.
(54) Massey, V. *J. Biol. Chem.* **1994**, *269*, 22459−22462.
(55) Ballou, D. P. Ph.D. Thesis, University of Michigan, 1971.
(56) SOD was not included in these experiments, as initial studies demonstrated that the reaction rates were affected only at the highest concentrations of SOD, 250 U/mL, and then only slightly (Figure S8B). We attribute the negligible effect of SOD in the presence of Mn^{II}-loaded NrdF to $O_2^{\bullet-}$ channeling to the metal site rather than its reacting further with NrdI.
(57) The monotonic increase in $NrdI_{sq}$ evident from the first ∼160 ms of the multiwavelength SF data (Figure 4A) suggests that the 8 s^{-1} phase corresponds to a second, slower phase of $NrdI_{sq}$ formation. The amplitude of the 8 s^{-1} phase is too large to be attributable to formation of $Mn^{III}Mn^{IV}$ intermediate, which does not absorb significantly at 610 nm (section 3.6.2), and 5 times too large to be attributable to formation of $Mn^{III}{}_2$ (ε_{610} = 0.25 mM^{-1} cm^{-1}) or $Mn^{III}{}_2$-Y• (ε_{610} = 0.3 mM^{-1} cm^{-1}).
(58) Studies of the dependence of these rate constants on $[O_2]$ (Figure S13) indicated that the 40 s^{-1} $NrdI_{sq}$ formation and 0.65 s^{-1} $NrdI_{sq}$ decay phases exhibited O_2 dependence, whereas the 8 s^{-1} $NrdI_{sq}$ rise phase did not. The latter observation is not understood at present but is likely related to reversibility of the reactions of NrdI with O_2. As expected if a metal-centered intermediate precedes tyrosine oxidation, the rate constant for formation of $Mn^{III}{}_2$ cluster and Y• (∼0.15 s^{-1} at 610 nm) was zero order in O_2.
(59) In support of the data fitting overestimating the value of k_1, a half-time of 11 to 16 ms for $NrdI_{sq}$ formation corresponds to a rate constant of 43−63 s^{-1}, in good agreement with the rate constant derived from the SF studies.
(60) Note that, even if the other 30% of $NrdI_{hq}$ reacts with O_2 to form H_2O_2 (the amplitudes of the SF fits suggest that all $NrdI_{hq}$ reacts to form $O_2^{\bullet-}$), only 15 μM H_2O_2 would be produced under these reaction conditions. This amount of H_2O_2 could only generate 7.5 μM Y•, whereas 27 μM is produced. This indicates that $O_2^{\bullet-}$ is the primary, and probably only, oxidant involved in cluster assembly.
(61) Khangulov, S. V.; Barynin, V. V.; Antonyuk-Barynina, S. V. *Biochim. Biophys. Acta* **1990**, *1020*, 25−33.
(62) Gelasco, A.; Kirk, M. L.; Kampf, J. W.; Pecoraro, V. L. *Inorg. Chem.* **1997**, *36*, 1829−1837.
(63) Zheng, M.; Khangulov, S. V.; Dismukes, G. C.; Barynin, V. V. *Inorg. Chem.* **1994**, *33*, 382−387.
(64) Gadda, G. *Biochemistry* **2012**, *51*, 2662−2669.
(65) Hoover, D. M.; Drennan, C. L.; Metzger, A. L.; Osborne, C.; Weber, C. H.; Pattridge, K. A.; Ludwig, M. L. *J. Mol. Biol.* **1999**, *294*, 725−743.
(66) Johansson, R.; Torrents, E.; Lundin, D.; Sprenger, J.; Sahlin, M.; Sjöberg, B. M.; Logan, D. T. *FEBS J.* **2010**, *277*, 4265−4277.
(67) Damiani, M. J.; Nostedt, J. J.; O'Neill, M. A. *J. Biol. Chem.* **2011**, *286*, 4382−4391.
(68) Meloon, D. R.; Wilkins, R. G. *Biochemistry* **1976**, *15*, 1284−1290.
(69) Teutloff, C.; Schäfer, K.-O.; Sinnecker, S.; Barynin, V.; Bittl, R.; Wieghardt, K.; Lendzian, F.; Lubitz, W. *Magn. Reson. Chem.* **2005**, *43*, S51−S64.
(70) Pick, M.; Rabani, J.; Yost, F.; Fridovich, I. *J. Am. Chem. Soc.* **1974**, *96*, 7329−7333.
(71) Bollinger, J. M., Jr.; Chen, S.; Parkin, S. E.; Mangravite, L. M.; Ley, B. A.; Edmondson, D. E.; Huynh, B. H. *J. Am. Chem. Soc.* **1997**, *119*, 5976−5977.
(72) Jiang, W.; Yun, D.; Saleh, L.; Barr, E. W.; Xing, G.; Hoffart, L. M.; Maslak, M. A.; Krebs, C.; Bollinger, J. M. J. *Science* **2007**, *316*, 1188−1191.
(73) Jiang, W.; Hoffart, L. M.; Krebs, C.; Bollinger, J. M., Jr. *Biochemistry* **2007**, *46*, 8709−8716.
(74) Andersson, C. S.; Öhrström, M.; Popović-Bijelić, A.; Gräslund, A.; Stenmark, P.; Högbom, M. *J. Am. Chem. Soc.* **2012**, *134*, 123−125.
(75) Dassama, L. M.; Boal, A. K.; Krebs, C.; Rosenzweig, A. C.; Bollinger, J. M., Jr. *J. Am. Chem. Soc.* **2012**, *134*, 2520−2523.
(76) Yun, D.; Krebs, C.; Gupta, G. P.; Iwig, D. F.; Huynh, B. H.; Bollinger, J. M., Jr. *Biochemistry* **2002**, *41*, 981−990.
(77) Roos, K.; Siegbahn, P. E. M. *J. Biol. Inorg. Chem.* **2011**, *16*, 553−565.
(78) Gunderson, W. A.; Zatsman, A. I.; Emerson, J. P.; Farquhar, E. R.; Que, L., Jr.; Lipscomb, J. D.; Hendrich, M. P. *J. Am. Chem. Soc.* **2008**, *130*, 14465−14467.
(79) Nordlund, P.; Eklund, H. *J. Mol. Biol.* **1993**, *232*, 123−164.
(80) Kauppi, B.; Nielsen, B. B.; Ramaswamy, S.; Larsen, I. K.; Thelander, M.; Thelander, L.; Eklund, H. *J. Mol. Biol.* **1996**, *262*, 706−720.